

1 **Dynamics-based estimates of decline trend with fine temporal variations in China's**  
2 **PM<sub>2.5</sub> emissions**

3  
4 **Zhen Peng<sup>1†</sup>, Lili Lei<sup>1,2†</sup>, Zhe-Min Tan<sup>1,2\*</sup>, Meigen Zhang<sup>3\*</sup>, Aijun Ding<sup>1</sup> and Xingxia Kou<sup>4</sup>**

5 <sup>1</sup>School of Atmospheric Sciences, Nanjing University, Nanjing 210093, China

6 <sup>2</sup>Key Laboratory of Mesoscale Severe Weather, Ministry of Education, Nanjing University,  
7 Nanjing 210093, China

8 <sup>3</sup>State Key Laboratory of Atmospheric Boundary Layer Physics and Atmospheric Chemistry,  
9 Institute of Atmospheric Physics, Chinese Academy of Sciences, Beijing 100029, China

10 <sup>4</sup>Institute of Urban Meteorology, China Meteorological Administration, Beijing 100089, China

11  
12 Corresponding author: Zhe-Min Tan (zmtan@nju.edu.cn) and Meigen Zhang  
13 (mgzhang@mail.iap.ac.cn)

14  
15 **Abstract**

16 Timely, continuous, and dynamics-based estimates of PM<sub>2.5</sub> emissions with a high temporal  
17 resolution can be objectively and optimally obtained by assimilating observed surface PM<sub>2.5</sub>  
18 concentrations using flow-dependent error statistics. [The annual dynamics-based estimates of](#)  
19 [PM<sub>2.5</sub> emission averaged over mainland China for years 2016-2020 without biomass burning](#)  
20 [emissions are 7.66, 7.40, 7.02, 6.62 and 6.38 Tg, respectively, which are very closed to the values](#)  
21 [of MEIC.](#) Annual PM<sub>2.5</sub> emissions in China have consistently decreased of approximately 3% to  
22 5% from 2017 to 2020. Significant PM<sub>2.5</sub> emission reductions occurred frequently in regions with  
23 large PM<sub>2.5</sub> emissions. COVID-19 could cause a significant reduction of PM<sub>2.5</sub> emissions in the  
24 north China plain and northeast of China in 2020. The magnitudes of PM<sub>2.5</sub> emissions were greater  
25 in the winter than in the summer. PM<sub>2.5</sub> emissions show an obvious diurnal variation that varies  
26 significantly with the season and urban population. [Compared to the diurnal variations of PM<sub>2.5</sub>](#)

27 emission fractions estimated based on diurnal variation profiles from US and EU, the estimated  
28 PM<sub>2.5</sub> emission fractions are 1.25% larger during the evening, the morning peak is 0.57% smaller  
29 in winter and 1.05% larger in summer, and the evening peak is 0.83% smaller. Improved  
30 representations of PM<sub>2.5</sub> emissions across time scales can benefit emission inventory, regulation  
31 policy and emission trading schemes, particularly for especially for high temporal resolution air  
32 quality forecasting and policy response to severe haze pollutions or rare human events with  
33 significant socioeconomic impacts.

## 35 1. Introduction

36 Anthropogenic emissions have imposed essential influences on the earth system, from  
37 hourly air quality and human health to long-time climate and environment. To reduce  
38 anthropogenic emissions, the Chinese government has enforced the Clean Air Action (2013) since  
39 2013. Studies to date that evaluated the emission controls and understood the climate responses  
40 from emission reductions often have used either a fixed meteorology with emission changes or  
41 *vice versa* (Li et al., 2019a; Li et al., 2021, Zhai et al., 2021). Estimated emissions from empirical  
42 extrapolation were commonly applied to analyze the meteorological-chemical mechanisms and  
43 associated social-economic impacts from occasional events like the 2015 China Victory Day  
44 Parade and Coronavirus Disease 2019 (COVID-19) pandemic (Wang et al., 2017; Liu et al., 2020;  
45 Huang et al., 2020; Zhu et al., 2021). But to better understand both long-term and short-term  
46 influences from emission changes, the continuous, up-to-date, and high temporal-/spatial-  
47 resolution emission estimates with coherent interactions of meteorology and emission changes are  
48 needed.

49 The complex contributions from energy production, industrial processes, transportation,  
50 and residential consumptions have imposed great challenges to accurately estimate the emissions.  
51 The emission inventories created by the traditional bottom-up techniques were typically outdated  
52 from the present day due to the lack of accurate and timely statistics, and often with coarse  
53 temporal resolutions from monthly to annual (Zhang et al., 2009; Li et al., 2014; Janssens-  
54 Maenhout et al., 2015; Zheng et al., 2018). Alternatively, update-to-date emission estimates with  
55 high temporal-spatial resolutions could be provided by top-down techniques (Miyazaki et al.,  
56 2017), but most emissions estimated by top-down techniques were intermittent and analyzed at

57 monthly scale or longer longer (Zhang et al., 2016; Jiang et al., 2017; Qu et al., 2017; Cao et al.,  
58 2018; Müller et al., 2018; Chen et al., 2019; Li et al., 2019b; Miyazaki et al., 2020). Moreover,  
59 emissions updated by the top-down techniques based on satellite observations could be insufficient  
60 to capture realistic near-surface characteristics (Li et al., 2019b; Liu et al., 2011; Choi et al., 2020).

61         Given the development of observation networks and advanced data assimilation strategies,  
62 timely and dynamics-based emission estimates with high temporal resolution can be achieved by  
63 harmonically constraining the atmospheric-chemical model with dense observations of trace gas  
64 compounds through an optimal assimilation methodology. The ensemble Kaman smoother (EnKS)  
65 (Whitaker et al., 2002; Peters et al., 2007; Peng et al., 2015), as a four-dimensional (4D)  
66 assimilation algorithm, makes use of chemical observations from past to future to provide an  
67 optimal estimate of source emissions, and it can capture the “error of the day” and construct fine  
68 emission characteristics with high temporal-spatial resolutions by using short-term ensemble  
69 forecasts (Kalnay, 2002). Since 2013, the fine particulate matter pollution (PM<sub>2.5</sub>, particles smaller  
70 than 2.5 μm in diameter) as the most urgent threat to public health has been persistently decreased,  
71 and ground-based observations of PM<sub>2.5</sub> have been progressively increased (Huang et al., 2018).  
72 Thus by harmonically assimilating dense surface PM<sub>2.5</sub> observations into an atmospheric-chemical  
73 model through an EnKS, hourly estimates of PM<sub>2.5</sub> emission that were continuously cycled for  
74 years 2016-2020 are presented in this study.

75         The timely estimated emissions can provide guidance for emission inventories that usually  
76 have time lags and emission trading schemes that often require up-to-date source emissions. Based  
77 on the dynamics-based estimated emissions with harmonic combination of the model and  
78 observations, better evaluation of the emission controls and more comprehensive understanding of  
79 the consequent climate responses can be obtained. The high temporal-resolution estimated  
80 emissions can reveal features of emissions that are absent from the traditional ones with coarse  
81 temporal resolutions. Moreover, the timely and dynamics-based emission estimates with high  
82 temporal resolution are essential for regional air quality modeling, especially for the occurrence of  
83 severe haze pollutions associated with timely evaluation for the impact on public health (Attri et  
84 al., 2001; Wang et al., 2014; Ji et al., 2018; Wang et al., 2020; Liu et al., 2021) and events that  
85 lead to large changes of emissions and significant socioeconomic impacts such as the COVID-19  
86 pandemic (Huang et al., 2020; Le et al., 2020).

## 87 2. Data assimilation and experimental design

88 The estimate of PM<sub>2.5</sub> emission can be successfully constrained by the PM<sub>2.5</sub> concentration  
89 observations through an ensemble Kalman filter (EnKF; Peng et al., 2017, 2018, 2020). For a  
90 retrospective ‘reanalysis’ mode here, all available PM<sub>2.5</sub> concentration observations, including  
91 those data collected after the analysis time, can be used. Thus a EnKS, a direct generalization of  
92 the EnKF, is applied to incorporate PM<sub>2.5</sub> concentration observations both before and after the  
93 analysis time, aiming to provide an optimal estimate of the PM<sub>2.5</sub> emission. In simple words, The  
94 emissions are updated by current and future observations though EnKS, while the concentrations  
95 are updated by current observations though EnKF. Detailed procedures of the EnKS are described  
96 in section 2.1.

### 97 2.1 An ensemble Kalman smoother to update the source emission

98 The ensemble priors of source emissions  $\mathbf{e}^f$  is created by multiplying a scaling factor  $\lambda^f$   
99 to the prescribed emission  $\mathbf{e}^p$  (Peng et al., 2017, 2018, 2020), where the superscript  $f$  denotes priors.  
100 Given a time-invariant constant  $\mathbf{e}^p$ , the update of  $\mathbf{e}^f$  is equivalent to the update of  $\lambda^f$ . Due to a  
101 time lag, the prior scaling factor at time  $t-1$  ( $\lambda_{t-1}^f$ ) is updated by chemical observations at time  $t$   
102 ( $\mathbf{y}_t^c$ ). At time  $t-1$ , the prior scaling factor for the  $i^{\text{th}}$  member is written as

$$103 \lambda_{i,t-1}^f = \frac{1}{M} \left[ \left( \beta \frac{\mathbf{c}_{i,t-1}^f}{\bar{\mathbf{c}}_{t-1}^f} + 1 - \beta \right) + \sum_{j=t-M}^{t-2} \lambda_{i,j|j+L:t-1}^a \right]. \quad (1)$$

104 The first term is the concentration ratio given by the prior of the chemical fields ( $\mathbf{c}_{i,t-1}^f$ ) normalized  
105 by the ensemble mean ( $\bar{\mathbf{c}}_{t-1}^f$ ), where  $\beta$  is an inflation factor used to compensate the insufficient  
106 ensemble spread (Peng et al., 2017). Through using the concentration ratio, each ensemble member  
107 of the source emissions naturally has the spatial correlations given by the chemical fields. The  
108 second term is the mean of the posterior scaling factors at previous assimilation cycles, where the  
109 superscript  $a$  denotes posteriors,  $M$  is the length of smoothing, and the subscript  $j+1:t-1$  indicates  
110 that the scaling factor at time  $j$  is updated by future observations from  $j+1$  to  $t-1$ . The assimilation  
111 of future observations will be described below.

112 The ensemble square-root filter (EnSRF) (Peng et al., 2017) is used to update  $\lambda_{t-1}^f$  by  
 113 assimilating  $\mathbf{y}_t^c$ . For the scaling factor at time  $t-1$ , posterior ensemble mean is given by

$$114 \quad \bar{\lambda}_{t-1}^a = \bar{\lambda}_{t-1}^f + \rho \circ \mathbf{P}_{t-1,t}^{ec} \mathbf{H}_t^{cT} \left( \mathbf{H}_t^c \mathbf{P}_t^c \mathbf{H}_t^{cT} + \mathbf{R}_t^c \right)^{-1} \left( \mathbf{y}_t^c - H_t^c \bar{\mathbf{c}}_t^f \right), \quad (2)$$

115 and posterior ensemble perturbations are given by

$$116 \quad \lambda_{i,t-1}^{\prime a} = \lambda_{i,t-1}^{\prime f} - \rho \circ \mathbf{P}_{t-1,t}^{ec} \mathbf{H}_t^{cT} \left[ \left( \sqrt{\mathbf{H}_t^c \mathbf{P}_t^c \mathbf{H}_t^{cT} + \mathbf{R}_t^c} \right)^{-1} \right]^T \left[ \sqrt{\left( \mathbf{H}_t^c \mathbf{P}_t^c \mathbf{H}_t^{cT} + \mathbf{R}_t^c \right) + \sqrt{\mathbf{R}_t^c}} \right]^{-1} \mathbf{H}_t^c \lambda_{i,t-1}^{\prime f},$$

117 (3)

118 where  $\mathbf{P}_{t-1,t}^{ec}$  denotes the background error covariance matrix of  $\lambda_{t-1}^f$  and  $\mathbf{c}_t^f$ ,  $\mathbf{P}_t^c$  indicates the  
 119 background error covariance matrix of  $\mathbf{c}_t^f$ ,  $H_t^c$ ,  $\mathbf{H}_t^c$  and  $\mathbf{R}_t^c$  are the observation forward operator,  
 120 Jacobian matrix and observation error covariance matrix of the chemical fields at time  $t$ ,  $\rho$  is the  
 121 localization matrix and  $\circ$  denotes the Schur (elementwise) product.

122 By applying the ensemble Kalman smoother (EnKS) (Whitaker et al., 2002; Peters et al.,  
 123 2007), the chemical observation  $\mathbf{y}_t^c$  is also assimilated to update the posterior scaling factor at  
 124 previous assimilation cycles  $j$  ( $j = t - K, \dots, t - 2$ ). After assimilating the future chemical  
 125 observation at time  $t$ , posterior ensemble mean of the scaling factor at  $j$  is given by

$$126 \quad \bar{\lambda}_{j,t+1}^a = \bar{\lambda}_{j,t+1}^a + \rho \circ \mathbf{P}_{j,t+1,t}^{ec} \mathbf{H}_t^{cT} \left( \mathbf{H}_t^c \mathbf{P}_t^c \mathbf{H}_t^{cT} + \mathbf{R}_t^c \right)^{-1} \left( \mathbf{y}_t^c - H_t^c \bar{\mathbf{c}}_t^f \right), \quad (4)$$

127 and posterior ensemble perturbations are given by

$$128 \quad \lambda_{i,j,t+1}^{\prime a} = \lambda_{i,j,t+1}^{\prime a} - \rho \circ \mathbf{P}_{j,t+1,t}^{ec} \mathbf{H}_t^{cT} \left[ \left( \sqrt{\mathbf{H}_t^c \mathbf{P}_t^c \mathbf{H}_t^{cT} + \mathbf{R}_t^c} \right)^{-1} \right]^T \left[ \sqrt{\left( \mathbf{H}_t^c \mathbf{P}_t^c \mathbf{H}_t^{cT} + \mathbf{R}_t^c \right) + \sqrt{\mathbf{R}_t^c}} \right]^{-1} \mathbf{H}_t^c \lambda_{i,t-1}^{\prime f}, \quad (5)$$

129 where  $\mathbf{P}_{j,t+1,t}^{ec}$  denotes the background error covariance matrix of  $\lambda_{j,t+1}^a$  and  $\mathbf{c}_t^f$ . After (2)-(5),  
 130 the updated  $\lambda_{j,t+1}^a$ ,  $j$  ( $j = t - M + 1, \dots, t - 1$ ) will be used to construct the prior scaling factor at next  
 131 time  $t+1$  (1).

132 As a Monte Carlo approach, the EnKS uses the forecast-analysis error covariances based  
133 on ensemble forecasts / analyses to compute the Kalman gain matrix with time lags, to incorporate  
134 observations from the past to the future. The first iteration of EnKS is equivalent to EnKF that  
135 assimilates observations up to the analysis time. The following iterations of EnKS assimilate  
136 observations in the future to update the state at the analysis time. The hourly forecasts of PM<sub>2.5</sub>  
137 concentration from the cycling assimilation experiment matched the independent observed  
138 quantities (Figure 1). Therefore, the ability of EnKS to retrieve the source emissions has been  
139 demonstrated. Previous studies also showed that simulations forced by the posterior emissions  
140 could produce improved forecasts for PM<sub>2.5</sub>, SO<sub>2</sub>, and NO<sub>2</sub> than those with a priori emissions  
141 (Peng et al., 2020).

## 142 2.2 WRF-Chem model, observations and emissions

143 To simulate the transport of aerosol and chemical species, the WRF-Chem model version  
144 3.6.1 (Grell et al., 2005) that has the meteorological and chemical components fully coupled is  
145 used. The model parameterization schemes follow Peng et al. (2017). Figure 2 shows the model  
146 domain that covers most east Asia regions. Horizontal grid spacing is 45 km with 57 vertical levels  
147 and model top at 10 hPa.

148 Experiments are conducted for each year from 2016 to 2020 separately. The 6-h  
149 meteorological observations, including all in-situ observations and cloud motion vectors from the  
150 National Centers for Environmental Prediction (NCEP) Global Data Assimilation System (GDAS;  
151 [http://www.emc.ncep.noaa.gov/mmb/data\\_processing/prepbuftr.doc/table\\_2.htm](http://www.emc.ncep.noaa.gov/mmb/data_processing/prepbuftr.doc/table_2.htm)), are assimilated  
152 every 6 h. The hourly observed chemical quantities, which contain PM<sub>10</sub>, PM<sub>2.5</sub>, SO<sub>2</sub>, NO<sub>2</sub>, O<sub>3</sub>,  
153 and CO from the Ministry of Ecology and Environment of China (<https://aqicn.org/map/china/cn/>),  
154 are assimilated every hour. Figure 2 shows the assimilated chemical observation network, which  
155 has 560 randomly chosen stations from 1576 stations in total. The thinning of observations is  
156 applied to avoid correlated errors of observations. The spatial autocorrelation of the thinning of  
157 observations is close to the original observations (Peng et al., 2017). The observation priors are  
158 computed by the “observer” portion of the Grid-point Statistical Interpolation system (GSI) (Kleist  
159 et al., 2009).

160 The hourly and ~~time-invariantly~~ constantly prescribed anthropogenic emissions are  
161 obtained from the EDGAR-HTAP (Emission Database for Global Atmospheric Research for

162 Hemispheric Transport of Air Pollution v2.2) v2.2 inventory (Janssens-Maenhout et al., 2015), in  
163 which the Chinese emissions are derived from MEIC in 2010 (Lei et al., 2011; Li et al., 2014).  
164 Natural emissions, including the biogenic (Guenther et al., 1995), dust (Ginoux et al., 2001),  
165 dimethyl sulfide and sea salt emissions (Chin et al., 2000), are computed online.

### 166 2.3 Assimilation and ensemble configurations

167 The  $PM_{2.5}$  emission directly gives the primary  $PM_{2.5}$ , and then the primary  $PM_{2.5}$  along  
168 with other precursor emissions could contribute to the secondary  $PM_{2.5}$ . The observations of  $PM_{2.5}$   
169 concentrations that contain both primary and secondary  $PM_{2.5}$ , are used to constrain the  $PM_{2.5}$   
170 emission through data assimilation. Thus the correlations between the concentration observations  
171 and source emissions might be contaminated by the secondary  $PM_{2.5}$ . Since the secondary  
172 formation process can be captured by the WRF-Chem model, the impact of the secondary  $PM_{2.5}$   
173 is indirectly considered. The detailed updated state variables with the according observations  
174 follow Peng et al. (2018). The concentrations and emissions of  $PM_{2.5}$ ,  $NH_3$ , and  $PM_{2.5}$  precursors  
175 that have observations ( $SO_2$  and  $NO$ ), are updated by the observed quantities, respectively, but the  
176 VOC that are also  $PM_{2.5}$  precursors are not updated due to the lack of direct and limited  
177 observations. In the present study, the impact of the secondary  $PM_{2.5}$  is ignored. One possible way  
178 to untangle the impact of secondary  $PM_{2.5}$  on the estimates of  $PM_{2.5}$  emission is to jointly estimate  
179 the source emission, primary and secondary  $PM_{2.5}$  given the concentration observations.

180 The National Oceanic and Atmospheric Administration (NOAA) operational EnKF system  
181 ([https://dtcenter.ucar.edu/com-GSI/users/docs/users\\_guide/GSIUserGuide\\_v3.7.pdf](https://dtcenter.ucar.edu/com-GSI/users/docs/users_guide/GSIUserGuide_v3.7.pdf)), which is an  
182 EnSRF and modified with the EnKS feature, is used to assimilate the observations. Ensemble size  
183 is set to 50. To combat the sampling error resulted from a limited ensemble size, covariance  
184 localization and inflation are applied. The Gaspari and Cohn (GC) (1999) function with a length  
185 scale of 675 km is used to localize the impact of observations and mitigate the spurious error  
186 correlations between observations and state variables. The constant multiplicative posterior  
187 inflation (Whitaker and Hamill 2012) with coefficients 1.12 for all meteorological and chemical  
188 variables is applied to enlarge the ensemble spread. The inflation  $\beta$  for advancing the scale factor  
189 is 1.2. The smoothing length  $M$  for source emissions is 4, and the EnKS lagged length  $K$  is 6. The  
190 larger the  $K$  value, the more future observations are assimilated to constrain the current emission  
191 estimate. But the sample estimated temporal correlations could be contaminated by sampling errors

192 and model errors, especially with increased lagged times. Thus, there is a tradeoff between the  
193 amount of future observations and accuracy of sample estimated temporal correlations. The choice  
194 of K (=6) is determined by sensitivity experiments.

195 At 0000 UTC 26 December of previous year, ensemble initial conditions (ICs) of the  
196 meteorological fields are generated by adding random perturbations that sample the static  
197 background error covariances (Barker et al., 2012) on the NCEP FNL (Final) analyses (Torn et al.,  
198 2006). Ensemble ICs of the chemical fields are 0, and source emissions of each ensemble member  
199 are adopted from the EDGAR-HTAP v2.2 inventory with random perturbations of mean 0 and  
200 variances of 10% of the emission values. Hourly ensemble lateral boundary conditions (LBCs) are  
201 generated using the same fixed-covariance perturbation technique as the ensemble ICs. After 6-d  
202 spin up, ensemble data assimilation experiments start cycling for each year.

### 203 3. PM<sub>2.5</sub> emission for years 2016-2020

204 Starting from the ~~time-invariant constant~~ source emission PR2010 (Janssens-Maenhout et  
205 al., 2015), the dynamics-based estimates of the PM<sub>2.5</sub> emissions are obtained, which include both  
206 the contributions of the anthropogenic and biomass burning emissions. The mean annual PM<sub>2.5</sub>  
207 emissions from biomass burning in China (2003~2017) was 0.51 Tg (Yin et al., 2019). ~~‡~~The annual  
208 dynamics-based estimates of PM<sub>2.5</sub> emission (DEPE) averaged over mainland China for years  
209 2016-2020 without biomass burning emissions are 7.66, 7.40, 7.02, 6.62, 6.17, 7.91, 7.53, 7.13 and  
210 6.38, 6.89 Tg, respectively. ~~For years 2016 and 2017, the annual DEPE are very closed to 8.1 and~~  
211 ~~7.6 Tg.~~ The values from the Multi-resolution Emission Inventory (MEIC; ) (Zheng et al., 2018) that  
212 does not consider the contributions of biomass burning emissions, are 8.10, 7.60, 6.70, 6.38 and  
213 6.04 Tg, respectively. Thus the annual DEPE are very closed to the values of MEIC. From year  
214 2017 to 2020, the estimated annual PM<sub>2.5</sub> emissions are reduced 3.4%, 8.4%, 13.6% and  
215 16.7% ~~3.2%, 7.8%, 12.7% and 15.7%~~ respectively compared to that of year 2016. There has been  
216 3%-5% persistent reduction of annual PM<sub>2.5</sub> emission from year 2017 to 2020, which demonstrates  
217 the effectiveness of China's Clean Air Action (2013) implemented since 2013 and China Blue Sky  
218 Defense War Plan (2018) enforced since 2018 with strengthened industrial emission standards,  
219 phased out outdated industrial capacities, promoted clean fuels in residential sector and so on  
220 (Zhang et al., 2019).

带格式的: 字体颜色: 文字 1



221 The monthly DEPE show reduction of PM<sub>2.5</sub> emission nearly in each month from years  
222 2016 to 2020 (Figure 3a), which further demonstrates the effectiveness of China's national plan,  
223 ~~rather than the role of weather effects alone~~. Compared to year 2016, both the reduction amount  
224 and reduction ratio of PM<sub>2.5</sub> emission are more prominent for February, March, June-September,  
225 and November than the other months (Figure3b). Given larger magnitudes of PM<sub>2.5</sub> emission in  
226 winter than in summer, emission controls with a focus from October to May should be considered  
227 in the design of future clean air actions in China, since total PM<sub>2.5</sub> emission during this period  
228 accounts for approximate 75% annual amount. Spatial distributions of the changes of PM<sub>2.5</sub>  
229 emission from year 2017 to 2020 compared to year 2016 show significant decreases occurred at  
230 Beijing-Tianjin-Hebei region (BTH), Yangtze River Delta region (YRD), Pearl River Delta region  
231 (PRD) and Sichuan-Chongqing Region (SCR), especially for years 2019-2020 (Figure 4). From  
232 year 2016 to 2020, BTH, YRD and SRC have larger reductions of PM<sub>2.5</sub> emission than PRD, but  
233 SCR has larger reduction ratio compared to year 2016 than BTH and YRD (Figure 5). Therefore,  
234 BTH and YRD have more potentials for PM<sub>2.5</sub> emission controls than PRD and SCR, which can  
235 give a guidance for future clean air actions. More specifically, most provinces have PM<sub>2.5</sub> emission  
236 reduction from year 2016 to 2020, and the reduction ratios generally increase from year 2017 to  
237 2020 (Table 1), which confirms continuous and effective emission controls from Clean Air Action  
238 to Blue Sky Defense War Plan in China. The monthly DEPE also demonstrates the effectiveness  
239 of strict implementations of emission reduction policies in China, such as the coal ban for  
240 residential heating since the 2017-2018 winter. There was a sharp change of PM<sub>2.5</sub> emission, from  
241 increase in 2017 to decrease in 2018. As shown by Figure 6, spatial distributions of the changes of  
242 PM<sub>2.5</sub> emissions in December compared to November in 2017 show obvious increases in most  
243 China. However, the changes in 2018 show significant decreases in areas of Beijing, Tianjin, Hebei,  
244 Shanxi, Henan and Anhui provinces due to the implementation of the coal ban.

245 Despites the trend in PM<sub>2.5</sub> emissions from year 2016 to 2020, the DEPE of year 2016 has  
246 similar monthly distributions to MEIC2016-2020 in general (Figure 3a). MEIC2016 has a “Pan-  
247 shape” monthly distribution with nearly ~~time-invariant~~ constant PM<sub>2.5</sub> emissions from April to  
248 October. This seasonal dependence of emissions is mainly contributed by the variations of  
249 residential energy use, which are empirically dependent on coarse monthly mean temperature  
250 intervals and thus cannot reflect the realistic monthly variations (Streets et al., 2003; Li et al., 2017).  
251 The centralized heating system in North China has a fixed date of turning-on and turning-off during

带格式的: 字体颜色: 红色

252 each heating season. Therefore, a sudden raise of emissions from October to November and a  
253 sudden drop of emissions from March to April are shown. But the turning-on and turning-off date  
254 are variable in different regions, which imposes a smoothing impact on the emissions. However,  
255 the DEPE yet shows a “V-shape” monthly distribution, with the minimum occurring in August.  
256 The estimated PM<sub>2.5</sub> emission is 11.8% higher than MEIC2016 in April but 12.1% lower than  
257 MEIC2016 in August, and these different monthly distributions can influence the consequent  
258 climate responses including the radiative forcing and energy budget (Yang et al., 2020) and also  
259 impact the health issues (Liu et al., 2018). Moreover, monthly fractions of the DEPE are consistent  
260 cross years (Figure 3c). The absence of interannual variations of monthly PM<sub>2.5</sub> emission fraction  
261 provides basis for previous studies that follow the same monthly changes of source emissions from  
262 different years (Zhang et al., 2009; Zheng et al., 2020, 2021). Monthly allocations of PM<sub>2.5</sub>  
263 emission can be directly and objectively obtained given an estimated total annual amount based  
264 on the estimated monthly fractions of DEPE, which is valuable for emission inventory, air quality  
265 simulation, and potentially applications for future scenarios due to more accurate month fractions  
266 of DEPE. Since the hourly priors of PM<sub>2.5</sub> concentrations from the cycling assimilation for  
267 optimally estimating PM<sub>2.5</sub> emission fit to the observed PM<sub>2.5</sub> quantities (Figure 1), the monthly  
268 DEPE provides more realistic monthly fluctuations than the empirical estimate.

#### 269 **4. Diurnal variations of PM<sub>2.5</sub> emission**

270 The DEPE with high temporal-resolution given the ~~time-invariant~~ constant prior PR2010  
271 can reveal features that are unable to represent in the commonly used emission estimates. Although  
272 the prior PR2010 has no diurnal variations, hourly posteriors of PM<sub>2.5</sub> emission provide the first  
273 objectively estimated diurnal variations for different seasons for years 2016-2020. However, these  
274 estimated diurnal variations include the contributions of the time-varying boundary layer. An  
275 observing system simulation experiment (OSSE) is performed to investigate the effects of the  
276 boundary layer. Details of this OSSE are presented in Appendix. The results indicate that the  
277 magnitude of posterior PM<sub>2.5</sub> emission from the OSSE is closer to the true emission than the prior.  
278 Since we have hourly assimilated observations to simultaneously update the chemical  
279 concentrations and source emissions, the impacts of time-varying boundary layer on the posterior  
280 PM<sub>2.5</sub> emissions are limited (Figures S1). A little larger estimated PM<sub>2.5</sub> emission fractions  
281 occurred in the morning and smaller estimated PM<sub>2.5</sub> emission fractions occurred in the afternoon.

带格式的: 字体颜色: 文字 1

带格式的: 字体颜色: 文字 1

282 comparing to the time-invariant true emission. Nevertheless, the influences of time-varying  
283 boundary layer are still important to PM<sub>2.5</sub> emission estimates. To statistically present the diurnal  
284 variations, the fractions of hourly PM<sub>2.5</sub> emissions divided by the daily amount are averaged over  
285 different years and regions after excluding the impacts of time-varying boundary layer (Figures 6  
286 7 and 78, and Table 2). The diurnal variations of PM<sub>2.5</sub> emission are critical for understanding the  
287 mechanisms of PM<sub>2.5</sub> formation and evolution and are also essential for PM<sub>2.5</sub> simulation and  
288 forecast.

289 Five-year mean diurnal variations of the estimated PM<sub>2.5</sub> emission fraction for mainland  
290 China show that despite the monthly variations of PM<sub>2.5</sub> emission, the diurnal-variation fractions  
291 for November, December, January and February are similar, while those for June, July and August  
292 are similar (Figure 6a7a). There are stronger diurnal variations of PM<sub>2.5</sub> emission in summer than  
293 in winter, which are represented by larger PM<sub>2.5</sub> emission fractions during morning and less PM<sub>2.5</sub>  
294 emission fractions during evening. The diurnal variations of PM<sub>2.5</sub> emission from March to May  
295 gradually transform from the patterns of winter to those of summer, and *vice versa* for the diurnal  
296 variations of PM<sub>2.5</sub> emission from September to November. The monthly changes of diurnal  
297 variations of PM<sub>2.5</sub> emission are consistent with the seasonal dependence, since monthly variations  
298 of PM<sub>2.5</sub> emission are mainly related to the variations of residential consumptions (Li et al., 2017)  
299 in which the space-heating has nearly no diurnal variations and then larger PM<sub>2.5</sub> emissions during  
300 winter lead to reduced diurnal variations than summer. Similar to the monthly fractions of  
301 estimated PM<sub>2.5</sub> emission for mainland China, diurnal variations of PM<sub>2.5</sub> emission fraction are  
302 consistent cross years for a given month (Figure 78). Table 2 gives five-year mean diurnal  
303 variations of the estimated PM<sub>2.5</sub> emission fraction for each month. Based on these high-resolution  
304 diurnal-variation fractions, hourly estimates of PM<sub>2.5</sub> emission can be objectively obtained for a  
305 given monthly estimated PM<sub>2.5</sub> emission.

306 Despite the high temporal resolution, the DEPE also has the ability to analyze diurnal  
307 variations for specific cities. The monthly changes of diurnal variations of PM<sub>2.5</sub> emission  
308 estimated for megacities with urban populations larger than 5 million and non-megacities with  
309 urban populations smaller than 5 million (Notice of the State Council on Adjusting the Standards  
310 for Categorizing City Sizes, 2014) are consistent with those estimated from mainland China  
311 (Figure 67). Compared to the diurnal variations of PM<sub>2.5</sub> emission estimated for mainland China,  
312 the megacities have stronger diurnal variations, while the non-megacities have weaker diurnal

313 variations. These detailed descriptions of PM<sub>2.5</sub> emission that are usually absent in common  
314 emission estimates can be essential for PM<sub>2.5</sub> simulation, especially for providing timely and  
315 realistic guidance for severe haze events.

316 There has been lack of local measurements for diurnal variations and widely adopted  
317 diurnal variation profiles of PM<sub>2.5</sub> emission in China. Compared to the diurnal variations of PM<sub>2.5</sub>  
318 emission fractions estimated based on diurnal variation profiles from US and EU (Wang et al.,  
319 2010; Du et al., 2020), the estimated PM<sub>2.5</sub> emission fractions are 1.25% larger during the evening,  
320 which greatly changes the diurnal variations of DEPE. The noon and evening peaks estimated  
321 from DEPE have smaller PM<sub>2.5</sub> emission fractions, with mean underestimations of PM<sub>2.5</sub> emission  
322 fraction of 0.340.40% and 1.050.83% for noon peak and evening peak respectively (Figures 6a-7a  
323 and 89). In fact, the smaller evening peaks of Wang et al. (2010) occurred in November, December,  
324 January, February and March, while they are almost indistinct from April to October, similar to  
325 that from DEPE. The morning peak of Wang et al. (2010) is similar to that of DEPE for spring and  
326 fall, but the former overestimates PM<sub>2.5</sub> emission fraction of 0.840.57% for winter while  
327 underestimates PM<sub>2.5</sub> emission fraction of 0.791.05% for summer. Due to the overestimated peaks,  
328 diurnal variations of Wang et al.(2010) have sharper appearance rate for morning peak and  
329 disappearance rate for evening peak. Compared to the diurnal variations based on diurnal variation  
330 profiles from ES and EU (Wang et al., 2010), the diurnal variations of the DEPE are constrained  
331 by the atmospheric-chemical model and observed PM<sub>2.5</sub> concentrations, which can objectively  
332 determine the diurnal variations of PM<sub>2.5</sub> emission for specific regions and seasons.

### 333 5. Impact of COVID-19 on PM<sub>2.5</sub> emissions

334 The abrupt outbreak of the COVID-19 pandemic has produced dramatically socioeconomic  
335 impacts in China. To prevent the virus spread, a lockdown was first implemented on 23 January  
336 2020 in Wuhan, Hubei province, and subsequently the national lockdown has been enforced in  
337 China (Liu et al., 2020; Huang et al., 2020; Zhu et al., 2021). Consequently, the total PM<sub>2.5</sub>  
338 emission of February 2020 for China shows an obvious decrease compared to those of previous  
339 years (Figure 3). The high temporal-resolution DEPE reveals the detailed changes of PM<sub>2.5</sub>  
340 emission with time (Figure 910). The PM<sub>2.5</sub> emission started to decrease right around the COVID  
341 outbreak, and had been smaller than those of year 2019 till early March. The emissions at the  
342 following months of 2020 are similar to those of 2019, due to the epidemic prevention and control

343 policies enforced by the China government. During February 2020, the DEPE shows significant  
344 reductions at the north China plain and northeast of China where prominent PM<sub>2.5</sub> emission  
345 occurred, while spotted PM<sub>2.5</sub> emission differences with small magnitudes showed at the other  
346 regions (Figures ~~10a11a~~-b). Along with recovery from the COVID-19, the estimated PM<sub>2.5</sub>  
347 emission rebounded in March (Figures 3a, ~~910~~, ~~10e11c~~-d), which is contributed to the national  
348 work resumption. Thus, the DEPE is able to timely reflect the dynamic response of PM<sub>2.5</sub> emission  
349 to the COVID-19.

350 To avoid fluctuations due to diurnal variations and monthly changes of PM<sub>2.5</sub> emission, 7-  
351 day averaged PM<sub>2.5</sub> emission differences between year 2020 and 2019 are used to analyze the  
352 dynamic impact of COVID-19 on PM<sub>2.5</sub> emission (Figure ~~1112~~). Before the lockdown, there were  
353 slight PM<sub>2.5</sub> emission differences over several provinces (Figures ~~11a12a~~-b). During the first week  
354 of lockdown, PM<sub>2.5</sub> emission reduction larger than  $5 \times 10^{-2}$  ( $\mu\text{g} \cdot \text{m}^{-2} \cdot \text{s}^{-1}$ ) that is about 60%-70%  
355 emission reduction, occurred at Hubei, Hunan, Guangdong, Anhui and Zhejiang provinces (Figure  
356 ~~11e12c~~). The PM<sub>2.5</sub> emission reduction extended to BTH and Shandong province during the  
357 second week of lockdown (Figure ~~11d12d~~), and continuously spread to the three northeast  
358 provinces of China during the third week of lockdown (Figure ~~11e12e~~). During the third week of  
359 lockdown, the increased PM<sub>2.5</sub> emissions for BTH and SCR are possibly caused by the long  
360 national vocation of spring holiday of year 2019~~massive emissions from high profile firework~~  
361 ~~burning on the Chinese New Year Eve of year 2019~~ (Ji et al., 2018). The inhomogeneous spatial  
362 variations of PM<sub>2.5</sub> emissions possibly relate with different traditions and policy enforcements for  
363 different provinces. The PM<sub>2.5</sub> emission reduction had been maintained over the central and  
364 northern China till early March when the lockdown was lift (Figures ~~11f12f~~-i). Though it is hard  
365 to see continuous and consistent signal of lockdown for the whole China~~Thus~~, the timely DEPE  
366 can provide up-to-date guidance for quantifying socioeconomic impacts from rare events with  
367 large emission changes such as the COVID-19.

368 Although there were significant reductions of PM<sub>2.5</sub> emissions over the central and northern  
369 China in February 2020, a severe air pollution event occurred over the north China in early  
370 February 2020. Previous studies have shown that the factors influencing the severe air pollution  
371 event include the still intensive emissions from industrial, power and residential, unfavorable  
372 meteorological condition, anomalously high humidity that promoted aerosol heterogeneous

373 chemistry, and secondary aerosol formation associated with increased atmosphere oxidants (Le et  
374 al. 2020; Sulaymon et al. 2021; Li et al., 2021) .

375

带格式的: 普通(网站), 缩进: 首行缩进: 1.27 厘米

## 376 **6. Discussion**

377 High temporal-resolution and dynamics-based estimations of PM<sub>2.5</sub> emission can be  
378 objectively and optimally obtained by assimilating past and future observed surface PM<sub>2.5</sub>  
379 concentrations through flow-dependent error statistics. This advanced assimilation strategy can be  
380 applied for emission estimates of other chemical species when corresponding observations are  
381 available, and extend to observation types besides the surface concentrations, like the aerosol  
382 optical depth (Liu et al., 2011; Choi et al., 2020). Moreover, current estimates of PM<sub>2.5</sub> emission  
383 are lack of explicitly representations of primary and secondary PM<sub>2.5</sub>, which could be resolved by  
384 joint estimation of the source emission, primary and secondary PM<sub>2.5</sub> given the concentration  
385 observations. Another deficiency of this top-down technique is that it cannot directly determine  
386 dynamics-based PM<sub>2.5</sub> emissions for different sectors and contributions from different policies,  
387 although the bottom-up technique has the potential to untangle the different contributions from  
388 different policies and quantify the different impacts on different sectors~~as the bottom-up~~  
389 ~~techniques.~~ However, But this top-down technique can be integrated into the bottom-up technique  
390 to retain advantages of both methods. One future work is to integrate the top-down technique with  
391 the bottom-up one, by which the emission estimates for different sectors and polices could be  
392 quantified. The annual emission estimate from the bottom-up technique can be further downscaled  
393 to hourly estimates by first distributing the annual amount to each month through the monthly  
394 allocations estimated from the top-down technique, and then assuming evenly daily distribution,  
395 finally applying the fractions of diurnal variation estimated from the top-down technique. The  
396 information collected by the bottom-up technique is retained, while the common drawback of  
397 coarse temporal resolution for the bottom-up technique is remedied. The integrated bottom-up and  
398 top-down technique can improve spatiotemporal representations of source emissions cross time  
399 scales and sectors, which is beneficial for emission inventory, air quality forecast, regulation policy  
400 and emission trading scheme.

401

## 402 **Acknowledgments**

403 This work is jointly sponsored by the National Key R&D Program of China through Grant  
404 2017YFC1501603 and the National Natural Science Foundation of China through Grants  
405 41922036 and 42275153. We are grateful to the High Performance Computing Center of Nanjing  
406 University for doing the cycling ensemble assimilation experiments.

## 407 **Data availability**

408 The meteorological data used for meteorological initial conditions and boundary conditions  
409 is available from the University Corporation for Atmospheric Research (UCAR) Research Data  
410 Archive (<https://rda.ucar.edu/datasets/ds083.3/>). The assimilated meteorological observations are  
411 available from the UCAR Research Data Archive (<https://rda.ucar.edu/datasets/ds337.0/>), and the  
412 assimilated chemical observations are available from <https://aqicn.org/map/china/cn/>. The  
413 prescribed ~~time-invariant~~ constant anthropogenic emissions are available from the Emission  
414 Database for Global Atmospheric Research for Hemispheric Transport of Air Pollution (EDGAR-  
415 HTAP) inventory ([https://data.jrc.ec.europa.eu/dataset/jrc-edgar-htap\\_v2-2](https://data.jrc.ec.europa.eu/dataset/jrc-edgar-htap_v2-2)) and the Multi-  
416 resolution Emission Inventory (MEIC; [http://meicmodel.org/?page\\_id=560](http://meicmodel.org/?page_id=560)).

417 The WRF-Chem model version 3.6.1 is available from  
418 [https://www2.mmm.ucar.edu/wrf/users/download/get\\_sources.html#WRF-Chem](https://www2.mmm.ucar.edu/wrf/users/download/get_sources.html#WRF-Chem). The NOAA  
419 operational EnKF system is available from [https://dtcenter.org/community-code/gridpoint-  
420 statistical-interpolation-gsi](https://dtcenter.org/community-code/gridpoint-statistical-interpolation-gsi).

421

## 422 **Competing interests**

423 The contact author has declared that none of the authors has any competing interests.

424

## 425 **References**

426 Attri, A. K., Kumar, U., and Jain, V. K.: Microclimate: formation of ozone by fireworks, *Nature*, 411, 1015,  
427 2001.

428 Barker, D., Huang, X.-Y., Liu, Z., Auligné, T., Zhang, X., Rugg, S., Ajjaji, R., Bourgeois, A., Bray, J., Chen,  
429 Y., Demirtas, M., Guo, Y.-R., Henderson, T., Huang, W., Lin, H.-C., Michalakes, J., Rizvi, S., and

430 Zhang, X.: The Weather Research and Forecasting Model's Community Variational/Ensemble Data  
431 Assimilation System: WRFDA, B. Am. Meteorol. Soc., 93, 831–843, [https://doi.org/10.1175/BAMS-](https://doi.org/10.1175/BAMS-D-11-00167.1)  
432 [D-11-00167.1](https://doi.org/10.1175/BAMS-D-11-00167.1), 2012.

433 Cao, H., Fu, T.-M., Zhang, L., Henze, D. K., Miller, C. C., Lerot, C., Abad, G. G., De Smedt, I., Zhang, Q., van  
434 Roozendaal, M., Hendrick, F., Chance, K., Li, J., Zheng, J., and Zhao, Y.: Adjoint inversion of Chinese  
435 non-methane volatile organic compound emissions using space-based observations of formaldehyde  
436 and glyoxal, *Atmos. Chem. Phys.*, 18, 15017–15046, <https://doi.org/10.5194/acp-18-15017-2018>, 2018.

437 Chen, C., Dubovik, O., Henze, D. K., Chin, M., Lapyonok, T., Schuster, G. L., Ducos, F., Fuertes, D., Litvinov,  
438 P., Li, L., Lopatin, A., Hu, Q., and Torres, B.: Constraining global aerosol emissions using  
439 POLDER/PARASOL satellite remote sensing observations, *Atmos. Chem. Phys.*, 19, 14585–14606,  
440 <https://doi.org/10.5194/acp-19-14585-2019>, 2019.

441 Chin, M., Rood, R. B., Lin, S. J., Muller, J. F., and Thompson, A. M.: Atmospheric sulfur cycle simulated in the  
442 global model GO-CART: Model description and global properties, *J. Geophys. Res.-Atmos.*, 105,  
443 24671–24687, 2000.

444 Choi, Y., Chen, S. H., Huang, C. C., Earl, K., Chen, C. Y., Schwartz, C. S., and Matsui, T.: Evaluating the impact  
445 of assimilating aerosol optical depth observations on dust forecasts over North Africa and the East  
446 Atlantic using different data assimilation methods, *Journal of Advances in Modeling Earth Systems*,  
447 12(4), e2019MS001890. <https://doi.org/10.1029/2019ms001890>, 2020.

448 [Du, Q., Zhao, C., Zhang, M., Dong, X., Chen, Y., Liu, Z., Hu, Z., Zhang, Q., Li, Y., Yuan, R., and Miao, S.:  
449 Modeling diurnal variation of surface PM<sub>2.5</sub> concentrations over East China with WRF-Chem: impacts  
450 from boundary-layer mixing and anthropogenic emission, \*Atmos. Chem. Phys.\*, 20, 2839–2863,  
451 <https://doi.org/10.5194/acp-20-2839-2020>, 2020.](#)

452 [Elbern, H., Strunk, A., Schmidt, H., and Talagrand, O.: Emission rate and chemical state estimation by 4-dimensional  
453 variational inversion, \*Atmos. Chem. Phys.\*, 7, 3749 – 3769, <https://doi.org/10.5194/acp-7-3749-2007>, 2007.](#)

454 Gaspari, G. and Cohn S. E.: Construction of correlation functions in two and three dimensions, *Q. J. Roy. Meteor.*  
455 *Soc.*, 125, 723–757, 1999.

456 Ginoux, P., Chin, M., Tegen, I., Prospero, J. M., Holben, B., Dubovik, O., and Lin, S.-J.: Sources and  
457 distributions of dust aerosols simulated with the GOCART model, *J. Geophys. Res.*, 106, 20255–20273,  
458 doi:10.1029/2000JD000053, 2001.

459 Grell, G., Peckham, S. E., Schmitz, R., McKeen, S. A., Frost, G., Skamarock, W. C., and Eder, B.: Fully coupled  
460 “online” chemistry within the WRF model, *Atmos. Environ.*, 39, 6957–6975,  
461 <https://doi.org/10.1016/j.atmosenv.2005.04.027>, 2005.

462 Guenther, A., Hewitt, C. N., Erickson, D., Fall, R., Geron, C., Graedel, T., Harley, P., Klinger, L., Lerdau, M.,  
463 McKay, W., Pierce, T., Scholes, B., Steinbrecher, R., Tallamraju, R., Taylor, J., and Zimmerman, P.: A  
464 global model of natural volatile organic compound emissions, *J. Geophys. Res.*, 100, 8873–8892,  
465 doi:10.1029/94JD02950, 1995.



466 Huang, X., Ding, A., Gao, J., Zheng, B., Zhou, D., Qi, X., Tang, R., Wang, J., Ren, C., Nie, W., Chi, X., Xu, Z.,  
467 Chen, L., Li, Y., Che, F., Pang, N., Wang, H., Tong, D., Qin, W., Cheng, W., Liu, W., Fu, Q., Liu, B.,  
468 Chai, F., Davis, S. J., Zhang, Q., and He, K.: Enhanced secondary pollution offset reduction of primary  
469 emissions during COVID-19 lockdown in China, *Natl. Sci. Rev.*, nwaal37,  
470 <https://doi.org/10.1093/nsr/nwaa137>, 2020.

471 Huang, J., Pan, X. C., Guo, X. B., and Li, G. X.: Health impact of China's Air Pollution Prevention and Control  
472 Action Plan: an analysis of national air quality monitoring and mortality data, *Lancet Planet. Health*, 2,  
473 E313–E323, [https://doi.org/10.1016/S2542-5196\(18\)30141-4](https://doi.org/10.1016/S2542-5196(18)30141-4), 2018.

474 Janssens-Maenhout, G., Crippa, M., Guizzardi, D., Dentener, F., Muntean, M., Pouliot, G., Keating, T., Zhang,  
475 Q., Kurokawa, J., Wankmüller, R., Denier van der Gon, H., Kuenen, J. J. P., Klimont, Z., Frost, G.,  
476 Darras, S., Koffi, B., and Li, M.: HTAP\_v2.2: a mosaic of regional and global emission grid maps for  
477 2008 and 2010 to study hemispheric transport of air pollution, *Atmos. Chem. Phys.*, 15, 11411–11432,  
478 <https://doi.org/10.5194/acp-15-11411-2015>, 2015.

479 Ji, D., Cui, Y., Li, L., He, J., Wang, L., Zhang, H., Wang, W., Zhou, L., Maenhaut, W., Wen, T., and Wang, Y.:  
480 Characterization and source identification of fine particulate matter in urban Beijing during the 2015  
481 Spring Festival, *Sci. Total Environ.*, 628–629, 430–  
482 440, <https://doi.org/10.1016/j.scitotenv.2018.01.304>, 2018.

483 Jiang, Z., Worden, J. R., Worden, H., Deeter, M., Jones, D. B. A., Arellano, A. F., and Henze, D. K.: A 15-year  
484 record of CO emissions constrained by MOPITT CO observations, *Atmos. Chem. Phys.*, 17, 4565–4583,  
485 <https://doi.org/10.5194/acp-17-4565-2017>, 2017.

486 Kalnay, E.: *Atmospheric modeling, data assimilation and predictability* (p. 341), Cambridge: Cambridge  
487 University Press, 2002.

488 Kleist, D. T., Parrish, D. F., Derber, J. C., Treadon, R., Errico, R. M., and Yang, R.: Improving incremental  
489 balance in the GSI 3DVAR analysis system, *Mon. Weather Rev.*, 137, 1046–1060,  
490 [doi:10.1175/2008MWR2623.1](https://doi.org/10.1175/2008MWR2623.1), 2009.

491 Le, T., Wang, Y., Liu, L., Yang, J., Yung, Y. L., Li, G., and Seinfeld, J. H.: Unexpected air pollution with marked  
492 emission reductions during the COVID-19 outbreak in China, *Science*, 702–706,  
493 <https://doi.org/10.1126/science.abb7431>, 2020.

494 Lei, Y., Zhang, Q., He, K. B., and Streets, D. G.: Primary anthropogenic aerosol emission trends for China,  
495 1990–2005, *Atmos. Chem. Phys.*, 11, 931–954, <https://doi.org/10.5194/acp-11-931-2011>, 2011.

496 Li, N., Tang, K., Wang, Y., Wang, J., Feng, W., Zhang, H., Liao, H., Hu, J., Long, X., and Shi, C.: Is the efficacy  
497 of satellite-based inversion of SO<sub>2</sub> emission model dependent? *Environmental Research Letters*, 16,  
498 035018, 2021.

499 Li, K., Jacob, D. J., Liao, H., Zhu, J., Shah, V., Shen, L., Bates, K. H., Zhang, Q., and Zhai, S.: A Two-Pollutant  
500 Strategy for Improving Ozone and Particulate Air Quality in China, *Nat. Geosci.*, 12, 906–  
501 910, <https://doi.org/10.1038/s41561-019-0464-x>, 2019a.

502 Li, J. and Wang, Y.: Inferring the anthropogenic NO<sub>x</sub> emission trend over the United States during 2003–2017  
503 from satellite observations: was there a flattening of the emission trend after the Great Recession? *Atmos.*  
504 *Chem. Phys.*, 19, 15339–15352, <https://doi.org/10.5194/acp-19-15339-2019>, 2019b.

505 Li, M., Zhang, Q., Kurokawa, J.-I., Woo, J.-H., He, K., Lu, Z., Ohara, T., Song, Y., Streets, D. G., Carmichael,  
506 G. R., Cheng, Y., Hong, C., Huo, H., Jiang, X., Kang, S., Liu, F., Su, H., and Zheng, B.: MIX: a mosaic  
507 Asian anthropogenic emission inventory under the international collaboration framework of the MICS-  
508 Asia and HTAP, *Atmos. Chem. Phys.*, 17, 935–963, <https://doi.org/10.5194/acp-17-935-2017>, 2017.

509 Li, M., Zhang, Q., Streets, D. G., He, K. B., Cheng, Y. F., Emmons, L. K., Huo, H., Kang, S. C., Lu, Z., Shao,  
510 M., Su, H., Yu, X., and Zhang, Y.: Mapping Asian anthropogenic emissions of non-methane volatile  
511 organic compounds to multiple chemical mechanisms, *Atmos. Chem. Phys.*, 14, 5617–  
512 5638, <https://doi.org/10.5194/acp-14-5617-2014>, 2014.

513 Liu, J., Yin, H., Tang, X., Zhu, T., Zhang, Q., Liu, Z., Tang, X., and Yi, H.: Transition in air pollution, disease  
514 burden and health cost in China: A comparative study of long-term and short-term exposure,  
515 *Environmental Pollution*, 277, 116770, 2021.

516 Liu, T., Wang, X. Y., Hu, J. L., Wang, Q., An, J. Y., Gong, K. J., Sun, J. J., Li, L., Qin, M. M., Li, J. Y.,  
517 Tian, J. J., Huang, Y. W., Liao, H., Zhou, M., Hu, Q. Y., Yan, R. S., Wang, H. L., and Huang, C.:  
518 Driving Forces of Changes in Air Quality during the COVID-19 Lockdown Period in the Yangtze River  
519 Delta Region, China, *Environ. Sci. Technol.*, 7, 779–786, <https://doi.org/10.1021/acs.estlett.0c00511>,  
520 2020.

521 Liu, T., Cai, Y., Feng, B., Cao, G., Lin, H., Xiao, J., Li, X., Liu, S., Pei, L., Fu, L., Yang, X., and Zhang, B.:  
522 Long-term mortality benefits of air quality improvement during the twelfth five-year-plan period in 31  
523 provincial capital cities of China, *Atmospheric Environment*, 173, 53–61,  
524 <https://doi.org/10.1016/j.atmosenv.2017.10.054>, 2018.

525 Liu, Z., Liu, Q., Lin, H. C., Schwartz, C. S., Lee, Y. H., and Wang, T.: Three-dimensional variational  
526 assimilation of MODIS aerosol optical depth: implementation and application to a dust storm over  
527 East Asia, *J. Geophys. Res.*, 116, D23206, <https://doi.org/10.1029/2011JD016159>, 2011.

528 Miyazaki, K., Bowman, K., Sekiya, T., Eskes, H., Boersma, F., Worden, H., Livesey, N., Payne, V. H., Sudo,  
529 K., Kanaya, Y., Takigawa, M., and Ogochi, K.: Updated tropospheric chemistry reanalysis and emission  
530 estimates, TCR-2, for 2005–2018, *Earth Syst. Sci. Data*, 12, 2223–2259, [https://doi.org/10.5194/essd-  
531 12-2223-2020](https://doi.org/10.5194/essd-12-2223-2020), 2020.

532 Miyazaki, K., Eskes, H., Sudo, K., Boersma, K. F., Bowman, K., and Kanaya, Y.: Decadal changes in global  
533 surface NO<sub>x</sub> emissions from multi-constituent satellite data assimilation, *Atmos. Chem. Phys.*, 17, 807–  
534 837, <https://doi.org/10.5194/acp-17-807-2017>, 2017.

535 Müller, J.-F., Stavrou, T., Bauwens, M., George, M., Hurtmans, D., Coheur, P.-F., Clerbaux, C., and Sweeney,  
536 C.: Top-Down CO Emissions Based on IASI Observations and Hemispheric Constraints on OH Levels,  
537 *Geophys. Res. Lett.*, 45, 1621–1629, <https://doi.org/10.1002/2017GL076697>, 2018.

538 Notice of the State Council on Adjusting the Standards for Categorizing City Sizes (in Chinese) (Chinese State  
539 Council, 2014); [http://www.gov.cn/zwqk/2013-09/12/content\\_2486773.htm](http://www.gov.cn/zwqk/2013-09/12/content_2486773.htm)

540 Peng, Z., Lei, L., Liu, Z., Liu, H., Chu, K., and Kou, X.: Impact of Assimilating Meteorological Observations  
541 on Source Emissions Estimate and Chemical Simulations, *Geophys. Res. Lett.*, 47,  
542 e2020GL089030, <https://doi.org/10.1029/2020GL089030>, 2020.

543 Peng, Z., Lei, L., Liu, Z., Sun, J., Ding, A., Ban, J., Chen, D., Kou, X., and Chu, K.: The impact of multi-species  
544 surface chemical observation assimilation on air quality forecasts in China, *Atmos. Chem. Phys.*, 18,  
545 17387–17404, <https://doi.org/10.5194/acp-18-17387-2018>, 2018.

546 Peng, Z., Liu, Z., Chen, D., and Ban, J.: Improving PM<sub>2.5</sub> forecast over China by the joint adjustment of initial  
547 conditions and source emissions with an ensemble Kalman filter, *Atmos. Chem. Phys.*, 17, 4837–  
548 4855, <https://doi.org/10.5194/acp-17-4837-2017>, 2017.

549 Peng, Z., Zhang, M., Kou, X., Tian, X., and Ma, X.: A regional carbon data assimilation system and its  
550 preliminary evaluation in East Asia, *Atmos. Chem. Phys.*, 15, 1087–1104, [https://doi.org/10.5194/acp-](https://doi.org/10.5194/acp-15-1087-2015)  
551 [15-1087-2015](https://doi.org/10.5194/acp-15-1087-2015), 2015.

552 Peters, W., Jacobson, A. R., Sweeney, C., Andrews, A. E., Conway, T. J., Masarie, K., Miller, J. B., Bruhwiler,  
553 L. M. P., Petron, G., Hirsch, A. I., Worthy, D. E. J., van der Werf, G. R., Randerson, J. T., Wennberg, P.  
554 O., Krol, M. C., and Tans, P. P.: An atmospheric perspective on North American carbon dioxide  
555 exchange: CarbonTracker, *P. Natl. Acad. Sci. USA*, 104, 18925–18930, 2007.

556 Qu, Z., Henze, D. K., Capps, S. L., Wang, Y., Xu, X., and Wang, J.: Monthly top-down NO<sub>x</sub> emissions for  
557 China (2005–2012): a hybrid inversion method and trend analysis, *J. Geophys. Res.*, 122, 4600–4625,  
558 <https://doi.org/10.1002/2016JD025852>, 2017.

559 Streets, D. G., Bond, T. M. L., Carmichael, G. R., Fernandes, S., Fu, Q., He, D., Klimont, Z., Nelson, S. M.,  
560 Tsai, N. Y., Wang, M. Q., Woo, J.-H., and Yarber, K. F.: An inventory of gaseous and primary aerosol  
561 emissions in Asia in the year 2000. *J. Geophys. Res.*, 108(D21), 8809, doi:10.1029/2002JD003093,  
562 2003.

563 [Sulaymon et al. 2021. Persistent high PM<sub>2.5</sub> pollution driven by unfavorable meteorological conditions during  
564 the COVID-19 lockdown period in the Beijing-Tianjin-Hebei region, China. \*Environmental  
565 Research\*. <https://doi.org/10.1016/j.envres.2021.111186>](https://doi.org/10.1016/j.envres.2021.111186)

566 Torn, R. D., Hakim, G. J., and Snyder, C.: Boundary conditions for limited-area ensemble Kalman filters, *Mon.  
567 Weather Rev.*, 134, 2490–2502, 2006.

568 Wang, H., He, X., Liang, X., Choma, E. F., Liu, Y., Shan, L., Zheng, H., Zhang, S., Nielsen, C. P., Wang, S.,  
569 Wu, Y., and Evans, J. S.: Health benefits of on-road transportation pollution control programs in China,  
570 *P. Natl. Acad. Sci. USA*, 117, 25370, <https://doi.org/10.1073/pnas.1921271117>, 2020.

571 Wang, G., Cheng, S. Y., Wei, W., Yang, X. W., Wang, X. Q., Jia, J., Lang, J. L., and Lv, Z.: Characteristics and  
572 emission reduction measures evaluation of PM<sub>2.5</sub> during the two major events: APEC and Parade, *Sci.  
573 Total Environ.*, 595, 81–92, <https://doi.org/10.1016/j.scitotenv.2017.03.231>, 2017.

带格式的: 字体: 五号, 非倾斜, 字体颜色: 文字 1

574 Wang, Z., Li, J., Wang, Z., Yang, W., Tang, X., Ge, B., Yan, P., Zhu, L., Chen, X., and Chen, H.: Modeling study  
575 of regional severe hazes over mid-eastern China in January 2013 and its implica- tions on pollution  
576 prevention and control, *Sci. China-Earth Sci.*, 57, 3–13, 2014.

577 Wang, X. Y., Liang, X. Z., Jiang, W. M., Tao, Z. N., Wang, J. X. L., Liu, H. N., Han, Z. W., Liu, S. Y., Zhang, Y. Y.,  
578 Grell, G. A., and Peckham, S. E.: WRF-Chem simulation of East Asian air quality: Sensitivity to temporal  
579 and vertical emissions distributions, *Atmos. Environ.*, 44, 660–669, 2010.

580 Whitaker, J. S. and Hamill, T. M.: Ensemble data assimilation without perturbed observations, *Mon. Weather Rev.*,  
581 130, 1913–1924, 2002.

582 Whitaker, J. S. and Hamill, T. M.: Evaluating methods to account for system errors in ensemble data assimilation,  
583 *Mon. Weather Rev.*, 140, 3078–3089, 2012.

584 Yang, Y., Ren, L., Li, H., Wang, H., Wang, P., Chen, L., Yue, X., and Liao, H.: Fast climate responses to aerosol  
585 emission reductions during the COVID-19 pandemic, *Geophys. Res. Lett.*, 47,  
586 e2020GL089788, <https://doi.org/10.1029/2020gl089788>, 2020.

587 Zhai, S., Jacob, D. J., Wang, X., Liu, Z., Wen, T., Shah, V., Li, K., Moch, J. M., Bates, K. H., Song, S., Shen,  
588 L., Zhang, Y., Luo, G., Yu, F., Sun, Y., Wang, L., Qi, M., Tao, J., Gui, K., Xu, H., Zhang, Q., Zhao, T.,  
589 Wang, Y., Lee, H. C., Choi, H., and Liao, H.: Control of particulate nitrate air pollution in China, *Nat.*  
590 *Geosci.*, 14, 1–7, 2021.

591 Zhang, Q., Zheng, Y., Tong, D., Shao, M., Wang, S., Zhang, Y., Xu, X., Wang, J., He, H., Liu, W., Ding, Y.,  
592 Lei, Y., Li, J., Wang, Z., Zhang, X., Wang, Y., Cheng, J., Liu, Y., Shi, Q., Yan, L., Geng, G., Hong, C.,  
593 Li, M., Liu, F., Zheng, B., Cao, J., Ding, A., Gao, J., Fu, Q., Huo, J., Liu, B., Liu, Z., Yang, F., He, K.,  
594 and Hao, J.: Drivers of Improved PM<sub>2.5</sub> Air Quality in China from 2013 to 2017, *P. Natl. Acad. Sci.*  
595 *USA*, 116, 24463–24469, <https://doi.org/10.1073/pnas.1907956116>, 2019.

596 Zhang, L., Shao, J. Y., Lu, X., Zhao, Y. H., Hu, Y. Y., Henze, D. K., Liao, H., Gong, S., and Zhang, Q.: Sources  
597 and processes affect-ing fine particulate matter pollution over North China: An adjoint analysis of the  
598 Beijing APEC period, *Environ. Sci. Technol.*, 50, 8731–8740, <https://doi.org/10.1021/acs.est.6b03010>,  
599 2016.

600 Zhang, Q., Streets, D. G., Carmichael, G. R., He, K. B., Huo, H., Kannari, A., Klimont, Z., Park, I. S., Reddy,  
601 S., Fu, J. S., Chen, D., Duan, L., Lei, Y., Wang, L. T., and Yao, Z. L.: Asian emis- sions in 2006 for the  
602 NASA INTEX-B mission, *Atmos. Chem. Phys.*, 9, 5131–5153, [https://doi.org/10.5194/acp-9-5131-](https://doi.org/10.5194/acp-9-5131-2009)  
603 2009, 2009.

604 Zheng, B., Zhang, Q., Geng, G., Chen, C., Shi, Q., Cui, M., Lei, Y., and He, K.: Changes in China's  
605 anthropogenic emissions and air quality during the COVID-19 pandemic in 2020, *Earth Syst. Sci. Data*,  
606 13, 2895–2907, <https://doi.org/10.5194/essd-13-2895-2021>, 2021.

607 Zheng, B., Geng, G., Ciais, P., Davis, S. J., Martin, R. V., Meng, J., Wu, N., Chevallier, F., Broquet, G., Boersma,  
608 F., van der A, R., Lin, J., Guan, D., Lei, Y., He, K., and Zhang, Q.: Satellite-based estimates of decline

609 and rebound in China's CO<sub>2</sub> emissions during COVID-19 pandemic, *Sci. Adv.*, 6,  
610 eabd4998, <https://doi.org/10.1126/sciadv.abd4998>, 2020.

611 Zheng, B., Tong, D., Li, M., Liu, F., Hong, C., Geng, G., Li, H., Li, X., Peng, L., Qi, J., Yan, L., Zhang, Y.,  
612 Zhao, H., Zheng, Y., He, K., and Zhang, Q.: Trends in China's anthropogenic emissions since 2010 as  
613 the consequence of clean air actions, *Atmos. Chem. Phys.*, 18, 14095–14111,  
614 <https://doi.org/10.5194/acp-18-14095-2018>, 2018.

615 Zhu, J., Chen, L., Liao, H., Yang, H., Yang, Y., and Yue, X.: Enhanced PM<sub>2.5</sub> Decreases and O<sub>3</sub> Increases in  
616 China during COVID-19 Lockdown by Aerosol-Radiation Feedback, *Geophys. Res. Lett.*, 48,  
617 e2020GL090260, <https://doi.org/10.1029/2020GL090260>, 2021.

618  
619

## 620 **Figures and Tables**

### 621 **Captions:**

622 **Figure 1.** Times series of hourly PM<sub>2.5</sub> concentration biases ( $\mu\text{g}\cdot\text{m}^{-3}$ ). The ensemble mean priors  
623 compared to the observed quantities for December of years 2016–2020 (gray and black), and the  
624 mean biases of years 2016–2020 (blue).

625 **Figure 2.** Model domain and observation sites for cycling assimilation. Red and blue dots denote  
626 the assimilated and unassimilated observational sites, respectively.

627 **Figure 3.** (a) Dynamics-based monthly PM<sub>2.5</sub> emission estimates ( $\text{Tg}\cdot\text{day}^{-1}$ ) summed over  
628 mainland China of each year from 2016 to 2020 (colored) and the estimated PM<sub>2.5</sub> emission from  
629 MEIC (gray); (b) Ratio of PM<sub>2.5</sub> emission changes between two adjacent years from year 2016 to  
630 2020 normalized by the PM<sub>2.5</sub> emission of year 2016; (c) Monthly fractions of dynamics-based  
631 PM<sub>2.5</sub> emission estimates for years 2016–2020 (light blue), the five-year mean fractions of  
632 dynamics-based monthly PM<sub>2.5</sub> emission estimates with bars denoting one standard deviation of  
633 the five-year variations (dark blue), and the monthly fractions of estimated PM<sub>2.5</sub> emission from  
634 MEIC (gray).

635 **Figure 4.** (a) Spatial distribution of dynamics-based PM<sub>2.5</sub> emission estimates ( $\mu\text{g}\cdot\text{m}^{-2}\cdot\text{s}^{-1}$ ) for  
636 year 2016, and compared to that of year 2016, spatial distributions of dynamics-based PM<sub>2.5</sub>  
637 emission changes of year (b) 2017, (c) 2018, (d) 2019 and (e) 2020.

638 **Figure 5.** (a) The differences of dynamics-based PM<sub>2.5</sub> emission estimates between years 2017–  
639 2020 and 2016, and (b) the differences normalized by that of year 2016.

640 **Figure 6.** Spatial distributions of dynamics-based PM<sub>2.5</sub> emission changes in December compared to November  
641 in (a) 2017 and (b) 2018.

642 **Figure 67.** Five-year mean diurnal variations of dynamics-based PM<sub>2.5</sub> emission fraction averaged  
643 over (a) mainland China, (b) megacities with urban population ≥ 5 million, and (c) non-megacities  
644 with urban population < 5 million.

645 **Figure 78.** Diurnal variations of dynamics-based PM<sub>2.5</sub> emission fractions for years 2016-2020  
646 (light blue) and five-year mean fractions with bars denoting one standard deviation of the five-  
647 year variations (dark blue) are averaged over mainland China for (a) January, (b) April, (c) July,  
648 and (d) October.

649 **Figure 89.** Diurnal variations of PM<sub>2.5</sub> emission fraction for each month based on diurnal variation  
650 profiles from ES and EU (Wang et al. 2010).

651 **Figure 910.** Hourly (light red and blue) and daily (dark red and blue) dynamics-based PM<sub>2.5</sub>  
652 emission estimates (kg·h<sup>-1</sup>) summed over mainland China from January to March of years 2019  
653 and 2020.

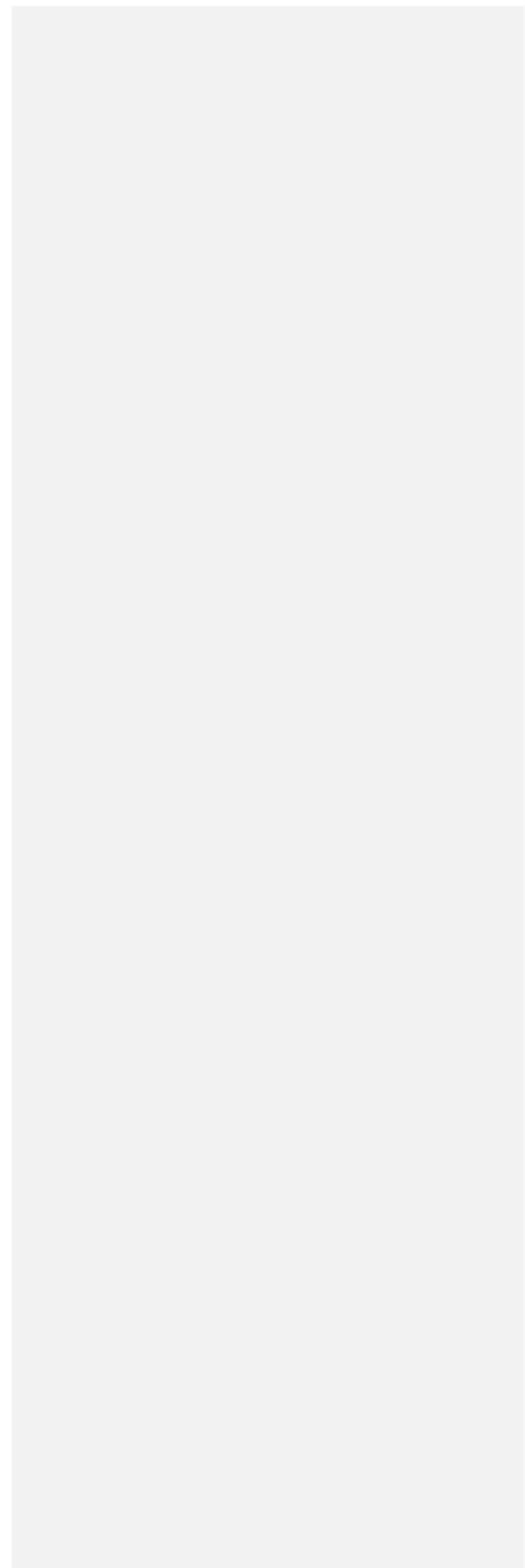
654 **Figure 1011.** Spatial distributions of dynamics-based PM<sub>2.5</sub> emission estimates (μg·m<sup>-2</sup>·s<sup>-1</sup>) on (b)  
655 February and (d) March of year 2019, and spatial distributions of dynamics-based PM<sub>2.5</sub> emission  
656 reduction of year 2020 compared to year 2019 for (c) February and (e) March.

657 **Figure 1112.** Mean spatial distributions of PM<sub>2.5</sub> emission differences (μg·m<sup>-2</sup>·s<sup>-1</sup>) between year  
658 2020 and 2019 for 9 weeks starting at 9 January 2020. Negative (positive) values indicate that  
659 PM<sub>2.5</sub> emission of year 2020 is smaller (larger) than that of year 2019. The numbers in (a) denote  
660 provinces as: 1 Heilongjiang, 2 Neimenggu, 3 Xinjiang, 4 Jilin, 5 Liaoning, 6 Gansu, 7 Hebei, 8  
661 Beijing, 9 Shanxi, 10 Tianjin, 11 Shanxi, 12 Ningxia, 13 Qinghai, 14 Shandong, 15 Xizang, 16  
662 Henan, 17 Jiangsu, 18 Anhui, 19 Sichuan, 20 Hubei, 21 Chongqing, 22 Shanghai, 23 Zhejiang, 24  
663 Hunan, 25 Jiangxi, 26 Yunnan, 27 Guizhou, 28 Fujian, 29 Guangxi, 30 Guangdong, 31 Taiwan,  
664 32 Hongkong, 33 Macao, 34 Hainan.

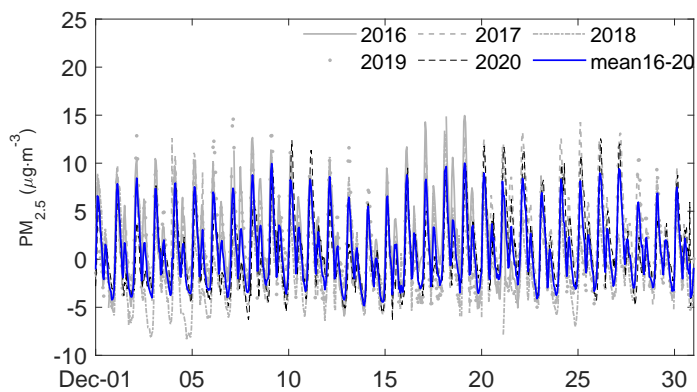
665 **Table 1.** Dynamics-based PM<sub>2.5</sub> emission estimates of year 2016 for each province whose value  
666 is larger than 0.01 μg·m<sup>-2</sup>·s<sup>-1</sup> are shown in the second column. Ratios of PM<sub>2.5</sub> emission changes  
667 of years 2017-2020 compared to year 2016 are shown from the third to the sixth column, with  
668 negative (positive) values indicating decrease (increase) of PM<sub>2.5</sub> emission.

669 **Table 2.** Five-year mean diurnal fractions (%) of the dynamics-based PM<sub>2.5</sub> emission estimates  
670 over mainland China on local solar time (LST) for each month.

带格式的: SM Text



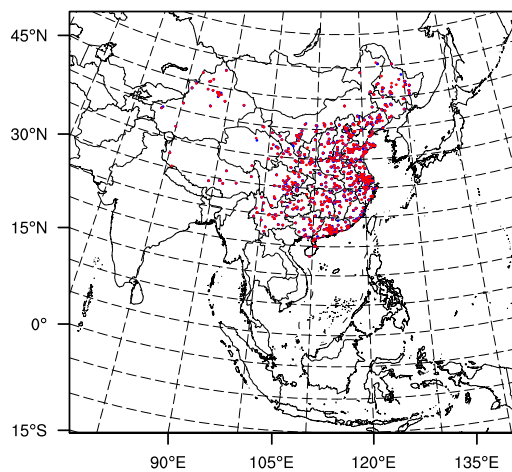
672  
673



674  
675 **Figure 1.** Times series of hourly PM<sub>2.5</sub> concentration biases (µg·m<sup>-3</sup>). The ensemble mean priors compared to  
676 the observed quantities for December of years 2016-2020 (gray and black), and the mean biases of years 2016-  
677 2020 (blue).  
678  
679  
680

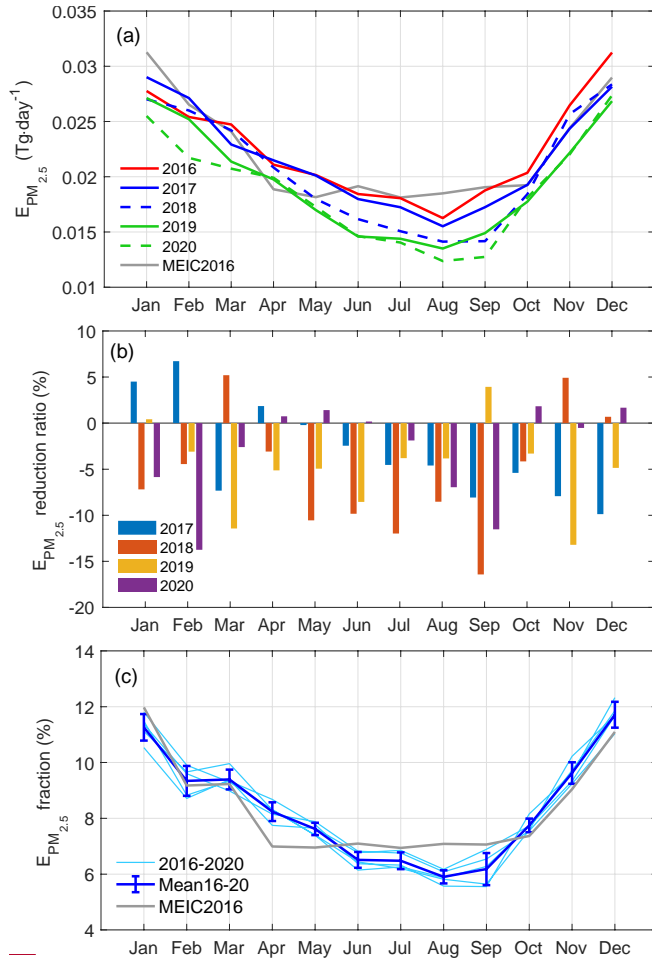


681



682  
683  
684  
685  
686

**Figure 2.** Model domain and observation sites for cycling assimilation. Red and blue dots denote the assimilated and unassimilated observational sites, respectively.



687

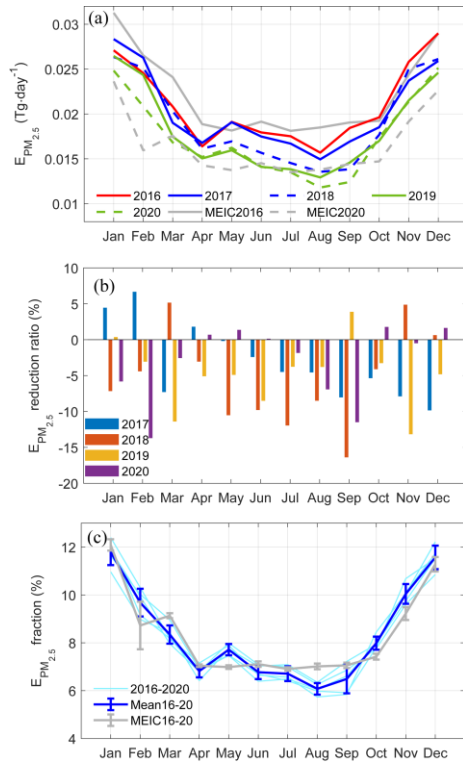


**Figure 3.** (a) Dynamics-based monthly  $PM_{2.5}$  emission estimates ( $Tg \cdot day^{-1}$ ) summed over mainland China of each year from 2016 to 2020 (colored) and the estimated  $PM_{2.5}$  emission from MEIC (gray); (b) Ratio of  $PM_{2.5}$  emission changes between two adjacent years from year 2016 to 2020 normalized by the  $PM_{2.5}$  emission of year 2016; (c) Monthly fractions of dynamics-based  $PM_{2.5}$  emission estimates for years 2016-2020 (light blue), the five-year mean fractions of dynamics-based monthly  $PM_{2.5}$  emission estimates with bars denoting one standard deviation of the five-year variations (dark blue), and the monthly fractions of estimated  $PM_{2.5}$  emission from MEIC (gray).

688  
689  
690  
691  
692  
693  
694  
695  
696  
697  
698  
699  
700  
701

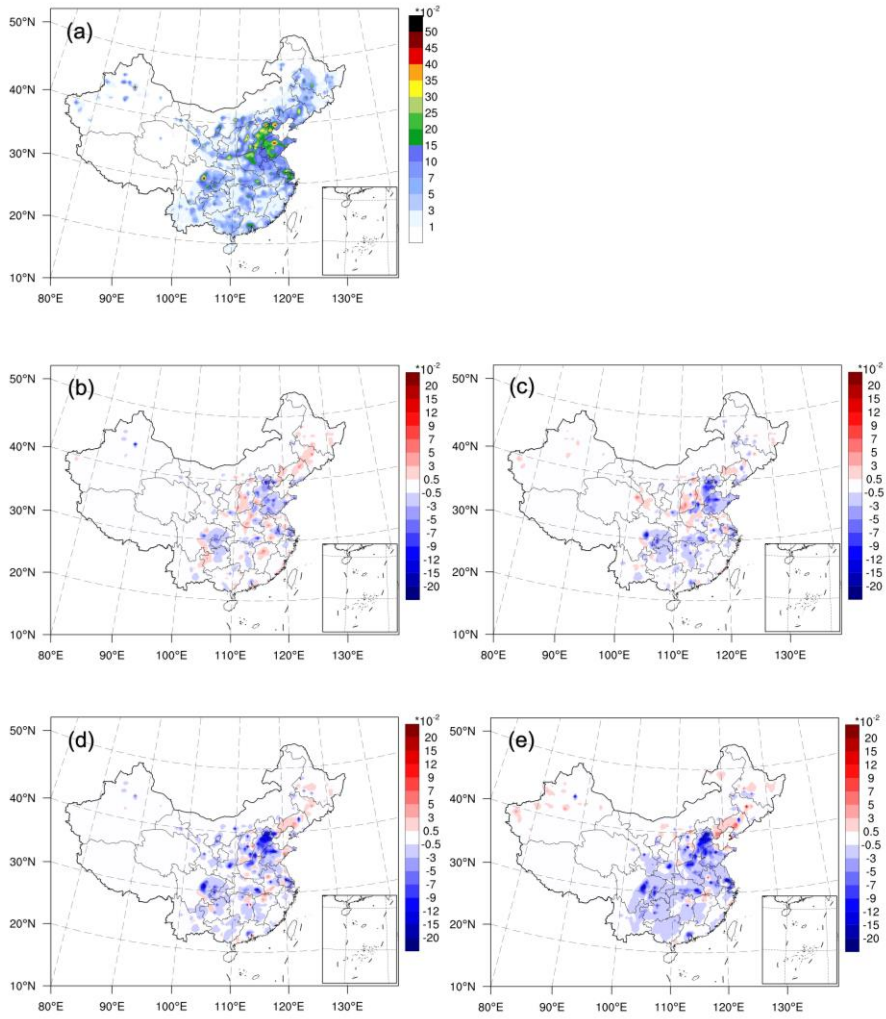
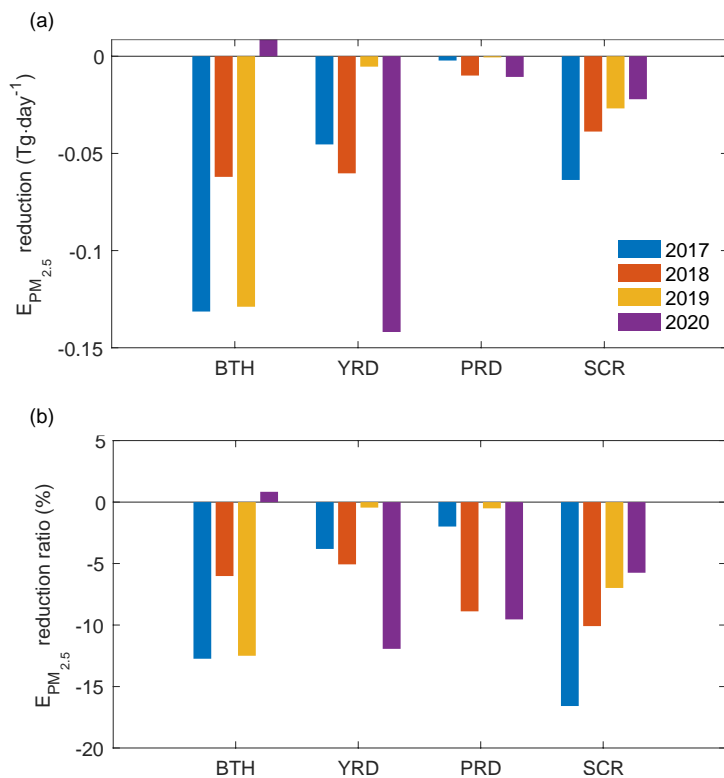


**Figure 4.** (a) Spatial distribution of dynamics-based PM<sub>2.5</sub> emission estimates ( $\mu\text{g}\cdot\text{m}^{-2}\cdot\text{s}^{-1}$ ) for year 2016, and compared to that of year 2016, spatial distributions of dynamics-based PM<sub>2.5</sub> emission changes of year (b) 2017, (c) 2018, (d) 2019 and (e) 2020.

702  
703  
704  
705  
706  
707  
708  
709

710



711 **Figure 5.** (a) The differences of dynamics-based PM<sub>2.5</sub> emission estimates between years 2017-2020 and 2016,  
712 and (b) the differences normalized by that of year 2016.  
713  
714  
715

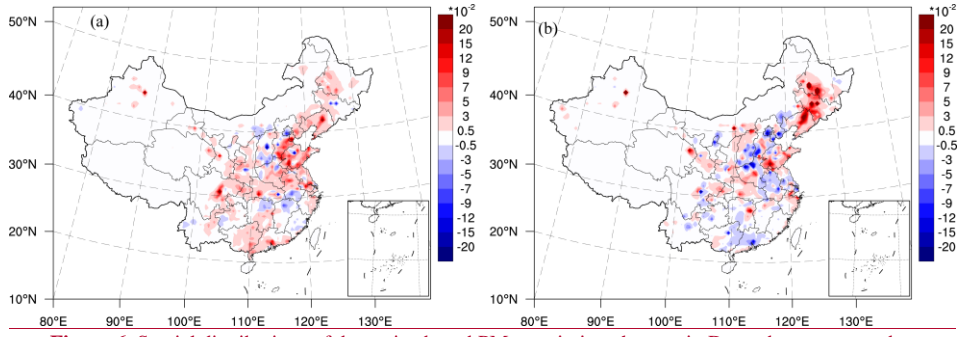
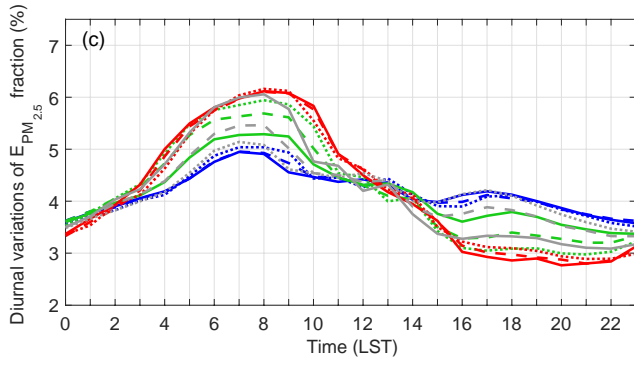
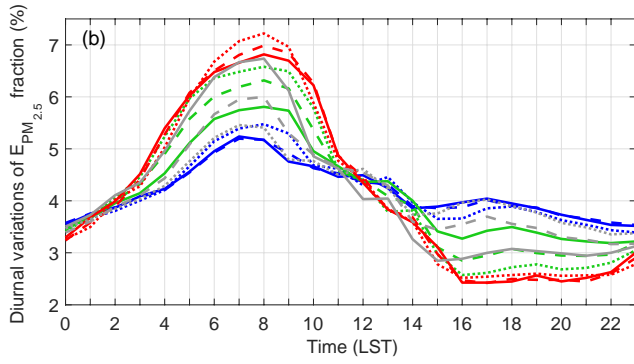
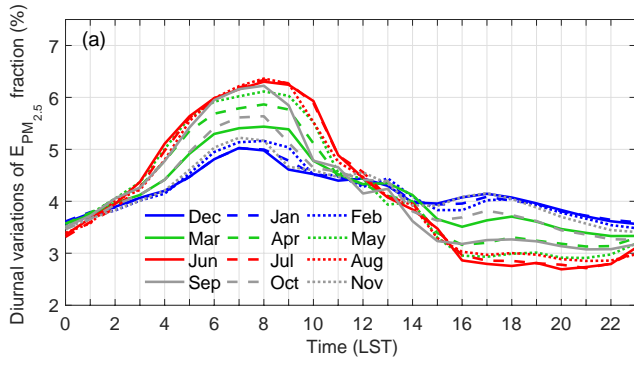


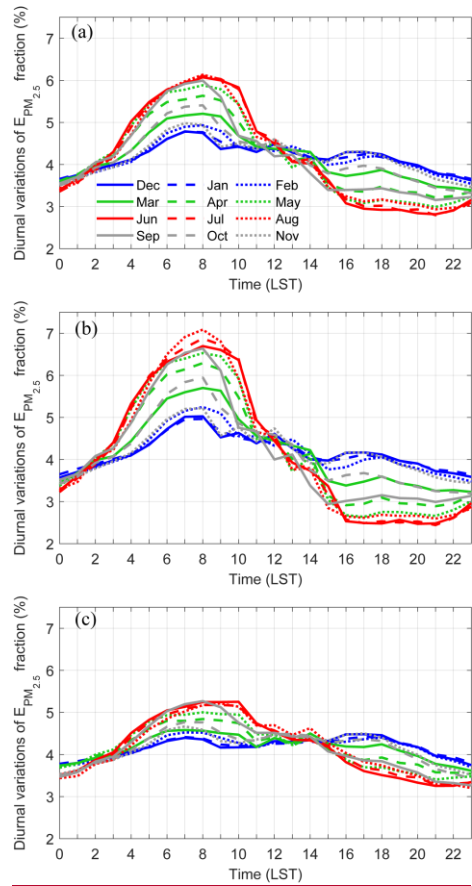
**Figure 6. Spatial distributions of dynamics-based PM<sub>2.5</sub> emission changes in December compared to November in (a) 2017 and (b) 2018.**

带格式的: 居中

716  
717  
718  
719  
720

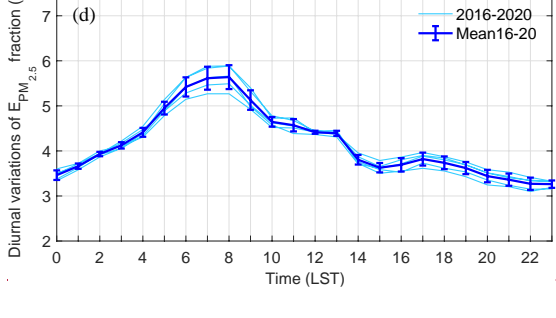
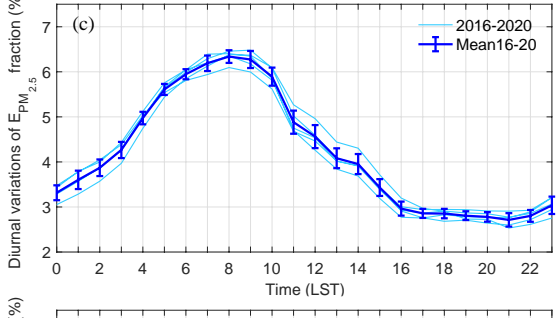
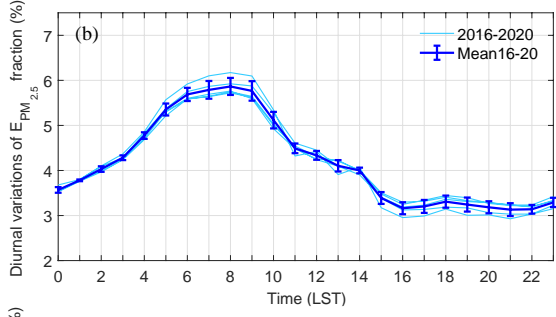
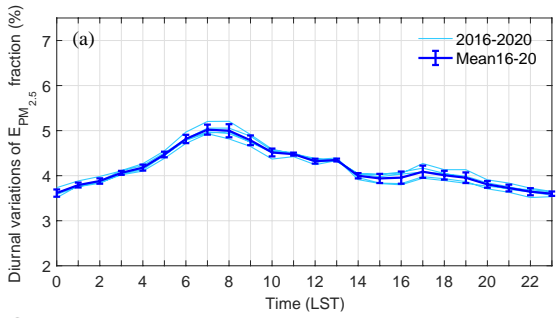


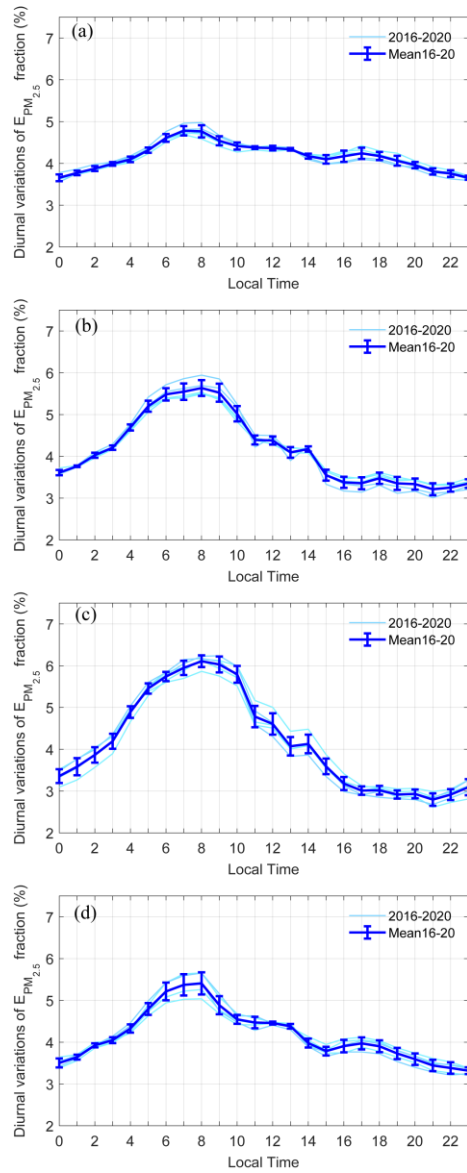
带格式的: 居中



722  
 723 **Figure 76.** Five-year mean diurnal variations of dynamics-based  $PM_{2.5}$  emission fraction averaged over (a) mainland  
 724 China, (b) megacities with urban population  $\geq 5$  million, and (c) non-megacities with urban population  $< 5$  million.



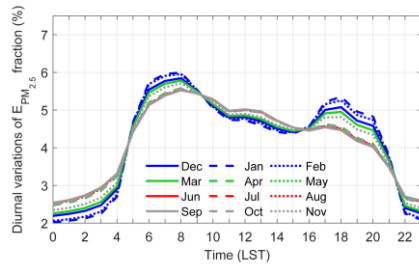




带格式的: 居中

726  
 727 **Figure 87.** Diurnal variations of dynamics-based PM<sub>2.5</sub> emission fractions for years 2016-2020  
 728 (light blue) and five-year mean fractions with bars denoting one standard deviation of the five-  
 729 year variations (dark blue) are averaged over mainland China for (a) January, (b) April, (c) July,  
 730 and (d) October.  
 731

732  
733  
734

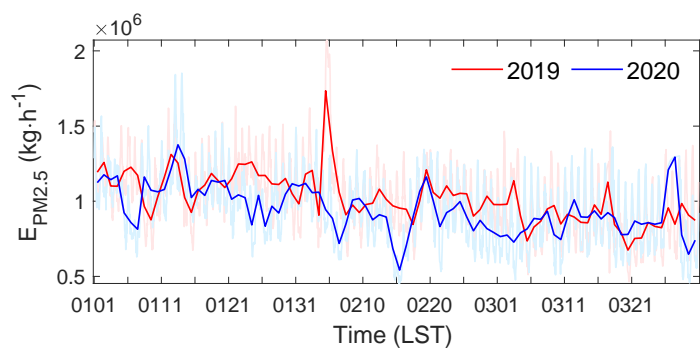


735  
736  
737  
738

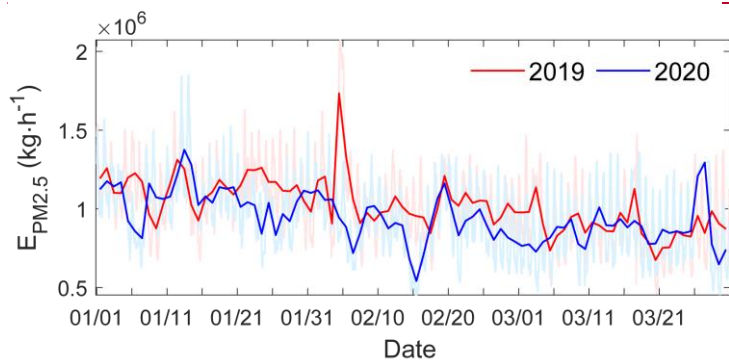
**Figure 89.** Diurnal variations of PM<sub>2.5</sub> emission fraction for each month based on diurnal variation profiles from ES and EU (Wang et al. 2010).

带格式的: 居中

739  
740



741

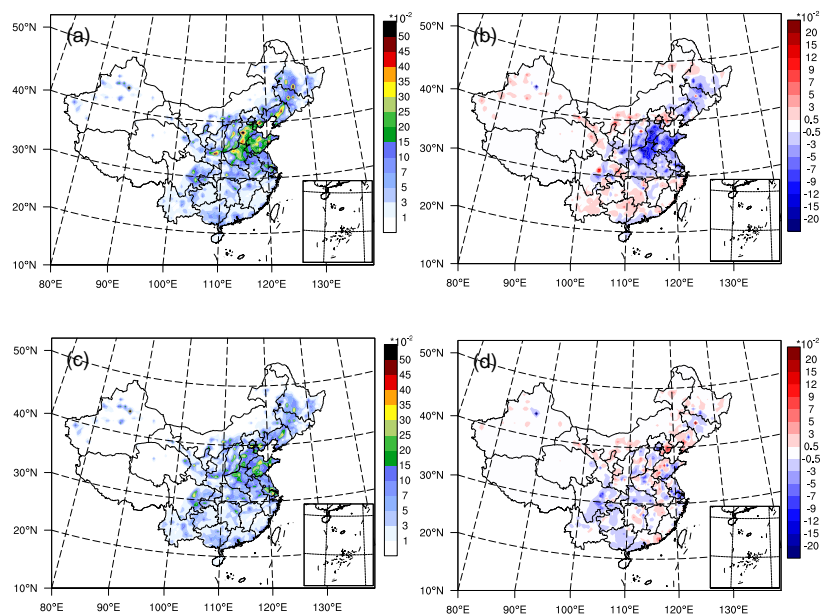


742

743 **Figure 910.** Hourly (light red and blue) and daily (dark red and blue) dynamics-based PM<sub>2.5</sub> emission estimates  
744 ( $\text{kg}\cdot\text{h}^{-1}$ ) summed over mainland China from January to March of years 2019 and 2020.

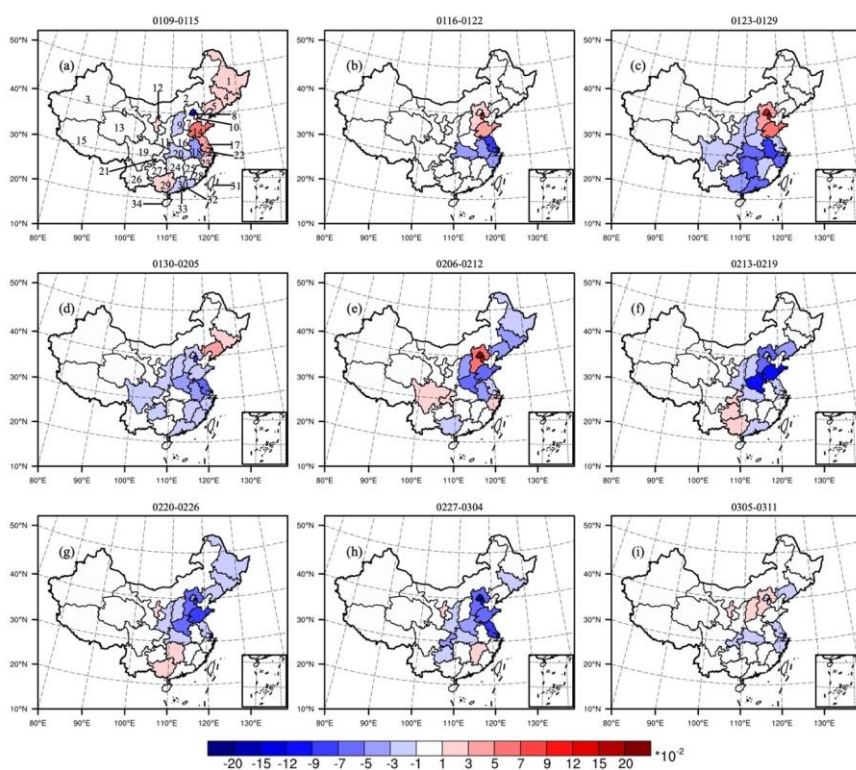
745

746



747  
748  
749  
750  
751  
752

**Figure 1011.** Spatial distributions of dynamics-based PM<sub>2.5</sub> emission estimates ( $\mu\text{g}\cdot\text{m}^{-2}\cdot\text{s}^{-1}$ ) on (b) February and (d) March of year 2019, and spatial distributions of dynamics-based PM<sub>2.5</sub> emission reduction of year 2020 compared to year 2019 for (c) February and (e) March.



754 **Figure 4.12.** Mean spatial distributions of PM<sub>2.5</sub> emission differences ( $\mu\text{g}\cdot\text{m}^{-2}\cdot\text{s}^{-1}$ ) between year  
 755 2020 and 2019 for 9 weeks starting at 9 January 2020. Negative (positive) values indicate that  
 756 PM<sub>2.5</sub> emission of year 2020 is smaller (larger) than that of year 2019. The numbers in (a) denote  
 757 provinces as: 1 Heilongjiang, 2 Neimenggu, 3 Xinjiang, 4 Jilin, 5 Liaoning, 6 Gansu, 7 Hebei, 8  
 758 Beijing, 9 Shanxi, 10 Tianjin, 11 Shanxi, 12 Ningxia, 13 Qinghai, 14 Shandong, 15 Xizang, 16  
 759 Henan, 17 Jiangsu, 18 Anhui, 19 Sichuan, 20 Hubei, 21 Chongqing, 22 Shanghai, 23 Zhejiang,  
 760 24 Hunan, 25 Jiangxi, 26 Yunnan, 27 Guizhou, 28 Fujian, 29 Guangxi, 30 Guangdong, 31  
 761 Taiwan, 32 Hongkong, 33 Macao, 34 Hainan.

762

763

764 **Table 1.** Dynamics-based PM<sub>2.5</sub> emission estimates of year 2016 for each province whose value  
 765 is larger than 0.01 μg·m<sup>-2</sup>·s<sup>-1</sup> are shown in the second column. Ratios of PM<sub>2.5</sub> emission changes  
 766 of years 2017-2020 compared to year 2016 are shown from the third to the sixth column, with  
 767 negative (positive) values indicating decrease (increase) of PM<sub>2.5</sub> emission.  
 768

Province	PM <sub>2.5</sub> emission of year 2016 (μg·m <sup>-2</sup> ·s <sup>-1</sup> )	Percentage of PM <sub>2.5</sub> emission change for year 2017 (%)	Percentage of PM <sub>2.5</sub> emission change for year 2018 (%)	Percentage of PM <sub>2.5</sub> emission change for year 2019 (%)	Percentage of PM <sub>2.5</sub> emission change for year 2020 (%)
Tianjin	0.2083	-14.07	-22.99	-38.70	-26.98
Shanghai	0.2067	-24.39	-30.21	-21.46	-30.05
Shandong	0.1631	-15.26	-21.02	-15.57	-19.41
Beijing	0.1598	-26.64	-25.75	-41.92	-45.27
Hebei	0.1178	-7.47	-11.98	-26.39	-22.87
Jiangsu	0.1088	-6.52	-3.98	-12.69	-28.20
Henan	0.1064	-1.41	-3.68	-12.15	-24.91
Shanxi	0.0885	<u>6.17</u>	<u>7.90</u>	-13.18	-13.85
Liaoning	0.0742	<u>6.32</u>	-2.58	<u>3.22</u>	<u>11.42</u>
Anhui	0.0687	<u>1.92</u>	-5.63	-6.23	-21.57
Hubei	0.0574	-5.87	-17.69	-19.76	-36.48
Zhejiang	0.0557	-3.62	-9.32	-9.99	-18.05
Chongqing	0.0525	-22.24	-29.81	-24.63	-38.41
Shanxi	0.0498	<u>0.62</u>	-1.97	-18.05	-17.85
Guangdong	0.0481	<u>1.21</u>	-6.01	-6.69	-14.37
Ningxia	0.0481	-8.17	-5.93	-24.46	-12.95
Hunan	0.0417	-6.40	-19.35	-9.91	-20.62
Guangxi	0.0390	-2.42	-3.52	-12.47	-22.31
Guizhou	0.0365	-4.01	-15.82	-21.74	-46.41
Jilin	0.0360	<u>12.30</u>	-3.22	<u>7.37</u>	<u>4.76</u>
Jiangxi	0.0353	<u>13.22</u>	-9.67	-7.19	-11.91
Sichuan	0.0337	-7.66	-15.66	-27.68	-37.93
Fujian	0.0244	<u>3.13</u>	-2.73	-8.13	-13.41
Heilongjiang	0.0231	<u>7.30</u>	-0.21	<u>3.14</u>	<u>3.91</u>
Yunnan	0.0221	-1.26	-7.16	-9.93	-15.35
Gansu	0.0177	-4.26	<u>5.28</u>	-17.89	-16.49
Hainan	0.0173	<u>3.93</u>	-0.41	-5.04	-4.78
Neimenggu	0.0141	-0.00	-3.63	-8.16	<u>3.55</u>

769  
770

771 **Table 2.** Five-year mean diurnal fractions (%) of the dynamics-based PM<sub>2.5</sub> emission estimates  
 772 over mainland China on local solar time (LST) for each month.

	Jan	Feb	Mar	Apr	May	Jun	Jul	Aug	Sep	Oct	Nov	Dec
0	3.65	3.58	3.61	3.61	3.55	3.40	3.36	3.44	3.55	3.50	3.53	3.63
1	3.77	3.69	3.72	3.76	3.74	3.65	3.58	3.56	3.70	3.64	3.64	3.75
2	3.88	3.82	3.96	4.03	4.05	3.94	3.86	4.01	4.05	3.93	3.83	3.89
3	3.98	3.94	4.05	4.21	4.29	4.30	4.19	4.14	4.19	4.05	3.93	3.99
4	4.10	4.06	4.33	4.69	4.92	5.03	4.89	4.71	4.69	4.33	4.12	4.12
5	4.32	4.38	4.76	5.20	5.46	5.48	5.45	5.39	5.27	4.80	4.45	4.32
6	4.61	4.74	5.09	5.48	5.72	5.78	5.74	5.78	5.74	5.21	4.83	4.61
7	4.78	4.90	5.17	5.55	5.78	5.92	5.95	5.98	5.92	5.37	4.98	4.79
8	4.77	4.93	5.21	5.63	5.88	6.07	6.11	6.13	5.99	5.41	4.94	4.75
9	4.54	4.79	5.14	5.52	5.79	6.00	6.03	6.02	5.60	4.89	4.42	4.37
10	4.41	4.41	4.68	5.02	5.43	5.83	5.79	5.42	4.68	4.55	4.50	4.42
11	4.38	4.40	4.42	4.39	4.45	4.79	4.78	4.66	4.56	4.47	4.36	4.30
12	4.37	4.32	4.37	4.38	4.48	4.49	4.61	4.51	4.19	4.46	4.60	4.48
13	4.34	4.43	4.34	4.09	3.93	4.06	4.07	4.09	4.23	4.38	4.33	4.29
14	4.17	4.26	4.30	4.18	4.16	4.02	4.13	4.10	3.79	3.98	4.10	4.15
15	4.10	3.99	3.82	3.55	3.46	3.63	3.59	3.45	3.39	3.79	4.07	4.12
16	4.17	4.05	3.73	3.38	3.17	3.08	3.18	3.24	3.40	3.92	4.30	4.29
17	4.24	4.17	3.79	3.36	3.08	2.95	3.01	3.12	3.41	3.98	4.31	4.30
18	4.18	4.21	3.87	3.48	3.16	2.92	3.03	3.17	3.44	3.91	4.21	4.24
19	4.06	4.04	3.72	3.35	3.12	2.92	2.93	3.08	3.34	3.73	3.99	4.07
20	3.96	3.93	3.62	3.34	3.07	2.84	2.93	3.04	3.29	3.59	3.85	3.98
21	3.81	3.75	3.47	3.21	2.99	2.83	2.80	2.93	3.16	3.44	3.65	3.79
22	3.76	3.66	3.44	3.25	3.09	2.91	2.92	2.97	3.19	3.38	3.56	3.73
23	3.65	3.55	3.39	3.34	3.23	3.16	3.09	3.04	3.23	3.32	3.47	3.62

773  
774

	Jan	Feb	Mar	Apr	May	Jun	Jul	Aug	Sep	Oct	Nov	Dec
0	3.61	3.53	3.57	3.57	3.50	3.36	3.33	3.39	3.51	3.46	3.49	3.59
1	3.79	3.71	3.74	3.78	3.76	3.67	3.60	3.58	3.72	3.66	3.66	3.77
2	3.88	3.82	3.97	4.03	4.05	3.95	3.87	4.01	4.05	3.93	3.83	3.89
3	4.06	4.02	4.12	4.28	4.37	4.37	4.27	4.22	4.26	4.12	4.01	4.07
4	4.18	4.15	4.42	4.78	5.01	5.11	4.97	4.80	4.77	4.41	4.21	4.20
5	4.47	4.53	4.92	5.35	5.61	5.64	5.61	5.55	5.42	4.95	4.60	4.47
6	4.82	4.95	5.30	5.69	5.92	5.98	5.95	5.98	5.95	5.42	5.04	4.81
7	5.02	5.14	5.41	5.79	6.02	6.16	6.19	6.22	6.16	5.61	5.22	5.03
8	5.00	5.16	5.44	5.87	6.12	6.30	6.34	6.36	6.22	5.64	5.17	4.98
9	4.78	5.04	5.39	5.77	6.03	6.24	6.27	6.27	5.85	5.13	4.66	4.61
10	4.51	4.51	4.78	5.12	5.53	5.93	5.89	5.52	4.78	4.66	4.60	4.52
11	4.48	4.50	4.52	4.49	4.55	4.89	4.88	4.76	4.66	4.57	4.46	4.40
12	4.32	4.28	4.33	4.34	4.43	4.45	4.56	4.47	4.15	4.42	4.56	4.44
13	4.35	4.44	4.35	4.10	3.94	4.07	4.08	4.10	4.24	4.39	4.34	4.30
14	4.00	4.09	4.12	4.00	3.99	3.84	3.95	3.93	3.62	3.80	3.93	3.98
15	3.94	3.83	3.66	3.39	3.30	3.48	3.43	3.29	3.24	3.63	3.91	3.96
16	3.96	3.83	3.51	3.16	2.95	2.86	2.96	3.03	3.18	3.69	4.09	4.08
17	4.09	4.02	3.63	3.20	2.93	2.80	2.86	2.97	3.25	3.82	4.16	4.15
18	4.01	4.05	3.70	3.31	2.99	2.76	2.85	3.00	3.27	3.74	4.05	4.07
19	3.95	3.93	3.61	3.24	3.01	2.82	2.81	2.97	3.23	3.62	3.88	3.96



20	3.81	3.78	3.46	3.18	2.92	2.69	2.78	2.89	3.14	3.44	3.70	3.83
21	3.73	3.67	3.39	3.13	2.91	2.74	2.71	2.85	3.08	3.36	3.57	3.71
22	3.64	3.54	3.33	3.14	2.98	2.79	2.80	2.86	3.08	3.27	3.45	3.62
23	3.60	3.48	3.33	3.29	3.18	3.10	3.04	2.98	3.17	3.26	3.41	3.56

775

776

777 **Appendix: Effects of meteorology**

778 An observing system simulation experiment (OSSE) is performed to investigate the effects of time-  
779 varying boundary layer. A nature run is first conducted from 0000 UTC 25 December 2015 to  
780 0000 UTC 2 February 2016, forced by the time-invariant source emissions PR2010 (the true  
781 emission). Synthetic observations of the six conventional air pollutant concentrations (i.e., PM<sub>10</sub>,  
782 PM<sub>2.5</sub>, SO<sub>2</sub>, NO<sub>2</sub>, O<sub>3</sub>, and CO) are generated from the natural run. Hourly synthetic observations  
783 are created from 0000 UTC 29 December 2015 to 0006 UTC 1 February 2016, by interpolating  
784 the gridded true surface concentrations to the chemical observation locations with additive random  
785 errors of  $N(0, R)$ .  $R$  is the observation error variance, which is calculated by the formula in Elbern  
786 et al. (2007). Outputs from the first four days of the natural run are excluded to avoid the transient  
787 effect. Then the prior emissions are generated by  $F^{pr} = (1.8 + \delta(x, y, z, t))F^r$ , where  $F^r$  is the true  
788 emission,  $\delta$  is a random number sampled from the normal distribution  $N(0,1)$  (Peng et al. 2015).  
789 Ensemble data assimilation experiments are conducted from 0000 UTC 29 December to 0006 UTC  
790 1 February 2016. Outputs from the first two days of the OSSE are excluded due to the spin-up.  
791 The magnitude of posterior PM<sub>2.5</sub> emission is closer to the true emission than the prior. Figure S1  
792 presents the monthly mean diurnal variations of PM<sub>2.5</sub> emission fraction from the OSSE. It shows  
793 that a little larger estimated PM<sub>2.5</sub> emission fractions occurred in the morning and smaller  
794 estimated PM<sub>2.5</sub> emission fractions occurred in the afternoon, comparing to the time-invariant true  
795 emission. But the diurnal variations of PM<sub>2.5</sub> emission fractions caused by the boundary layer are  
796 not as strong as that caused by the emission itself (Figure 7). The reason may be that we have  
797 hourly assimilated observations to simultaneously update the chemical concentrations and source  
798 emissions. Therefore, the impacts of time-varying boundary layer on the posterior PM<sub>2.5</sub> emissions  
799 are limited.

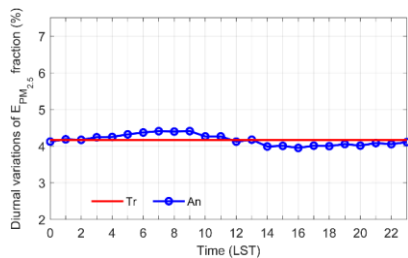
域代码已更改

域代码已更改

域代码已更改

域代码已更改

域代码已更改



800

801 **Figure S1. Diurnal variations of PM<sub>2.5</sub> emission fraction for the Observing System Simulation**

802 Experiment.

带格式的: SM Text, 居中

带格式的: 字体: (中文) 宋体, 小四